Coordination Chemistry Reviews 340 (2017) 79–97

Contents lists available at ScienceDirect

Coordination Chemistry Reviews

journal homepage: www.elsevier.com/locate/ccr

Review

Taking a last look at lanthanidomesogens? The use of basic thermodynamics for programming the temperature domains of existence of luminescent liquid crystals

Sebastiano Guerra [a], Thibault Dutronc [a], Emmanuel Terazzi [a], Kerry-Lee Buchwalder [a], Laure Guénée [b], Robert Deschenaux [c], Svetlana V. Eliseeva [d], Stéphane Petoud [a,d,*], Claude Piguet [a,*]

[a] Department of Inorganic and Analytical Chemistry, University of Geneva, 30 quai E. Ansermet, CH-1211 Geneva 4, Switzerland
[b] Laboratory of X-ray Crystallography, University of Geneva, 24 quai E. Ansermet, CH-1211 Geneva 4, Switzerland
[c] Laboratoire de chimie macromoléculaire, Institut de Chimie, Université de Neuchâtel, Avenue de Bellevaux 51, CH-2000 Neuchâtel, Switzerland
[d] Centre de Biophysique Moléculaire, CNRS UPR 4301, Rue Charles-Sadron, 45071 Orléans Cedex 2, France

ARTICLE INFO

Article history:
Received 19 September 2016
Received in revised form 18 November 2016
Accepted 18 November 2016
Available online 19 November 2016

Keywords:
Liquid crystals
Mesogens
Lanthanide
Thermodynamics
Cohesive energy densities
Luminescence

ABSTRACT

As for any thermotropic liquid crystals (often referred to as mesogens), those containing transition metals (metallomesogens), and more specifically lanthanides (lanthanidomesogens) would benefit from rational correlations between the microscopic variations introduced by chemists in their molecular structures and some planned macroscopic properties such as temperature domain of existence, viscosity and supramolecular organization. The novel concept of cohesive free energy density (CFED) allows the building of pseudo-phase boundaries, which connect chemical perturbations, usually measured with the help of arbitrary structural parameters, into quantitative pressure increments relevant to those found in pressure-temperature phase diagrams. With the help of this novel toolkit, cyanobiphenyl-based dendrimeric tridentate ligands have been used as a proof-of-concept for exploring the consequences of (i) the successive methylation of polyaromatic termini, (ii) the complexation to luminescent europium carriers and (iii) the statistical doping with structural defects on the thermodynamic parameters which control the phase transitions.

Contents

1. Introduction and background

The rational and theoretical modelling of intermolecular forces, which are responsible for the cohesion and organization of polymers, liquid crystals and soft matter, were initiated before the second world war [1] and reached an indisputable scientific recognition with the Nobel Prizes delivered to P. J. Flory in chemistry (1974) [2] and to P. G. de Gennes in physics (1991) [3]. Among the wealth of innovative concepts introduced during this period, the programming of the temperature domain of existence of thermotropic liquid crystals combined with the control of the supramolecular organization induced in the various thermotropic

* Corresponding authors at: Department of Inorganic and Analytical Chemistry, University of Geneva, 30 quai E. Ansermet, CH-1211 Geneva 4, Switzerland.
E-mail address: Claude.Piguet@unige.ch (C. Piguet).

http://dx.doi.org/10.1016/j.ccr.2016.11.013
0010-8545/

liquid-crystalline phases, often referred to as mesophases, appeared to be crucial for application-oriented research [4]. Standard *P-T* phase diagrams predicting the dependence of the transition temperatures under variable external pressures were thus built for the famous series of fluidic room-temperature liquid-crystalline 4′-*n*-alkyl-4-cyanobiphenyls (Fig. 1a) [5]. These data could be quantitatively analyzed within the frame of Clapeyron Eq. (1) making available the enthalpy (ΔH_{tr}), entropy (ΔS_{tr}) and volume (ΔV_{tr}) of transition for further tuning and programming [6].

$$\frac{dP}{dT} = \frac{\Delta S_{tr}}{\Delta V_{tr}} = \frac{\Delta H_{tr}}{T\Delta V_{tr}} \Rightarrow dP = \frac{\Delta H_{tr}}{\Delta V_{tr}} \cdot \frac{dT}{T} \Rightarrow P = P^* + \frac{\Delta H_{tr}}{\Delta V_{tr}} \ln\left(\frac{T}{T^*}\right) \quad (1)$$

As expected for the minor changes in volume accompanying the melting of solids or of liquid crystals (ΔV_{tr} is small in Eq. (1)), the associated phase boundaries display steep *dP*/*dT* slopes and only limited variations of the transition temperatures can be induced, and this even upon massive pressure changes (more than 1000 atmospheres are applied in Fig. 1a) [6]. Beyond the search for appealing macroscopic signatures (viscosity, birefringence, etc...) produced by different supramolecular organizations in soft matter [7], synthetic and material chemists rapidly realized that the chemical modifications of their preferred amphipathic molecules drastically influenced the transition temperatures which limit the domain of existence of the mesophase [8]. The quantitative pressure increments plotted as the ordinate axis in a standard *P*/*T* diagrams were thus replaced with some qualitative structural parameters pertinent to the imposed chemical perturbation of the system as illustrated in Fig. 1b, where the transition temperatures were reported as a function of the number of methylene rotors *n* in the terminal alkyl chains bound to tetracatanar-2,2′-bi pyridines [9]. When physicists consider this procedure, they are reluctant to adopt the latter intuitive short-cut and prefer to rigorously explore the effects of real external pressure increments on phase transition temperatures, which are thus specifically determined for each substituted 4′-*n*-alkyl-4-caynobiphenyls (the investigation of $5 \leqslant n \leqslant 8$ therefore requires three additional *P-T* phase diagrams similar to that depicted in Fig. 1a) [5]. During this systematic work, they interestingly noticed that the magnitude of the slopes of the phase boundary *dP*/*dT* for the nematic → isotropic phase boundaries regularly oscillated with the number of methylene rotors in the alkyl chains. The same conclusion could be reached with much less efforts by chemists, who simply showed that the magnitude of the clearing temperature T_c associated with the nematic → isotropic phase transition for each compound recorded under atmospheric pressure alternated with the number

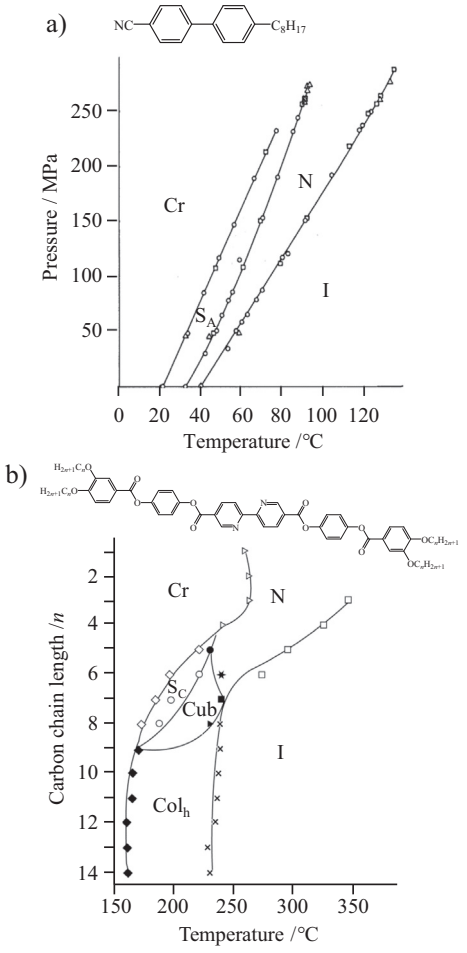

Fig. 1. (a) Physical pressure-temperature (*P-T*) phase diagram built for octylcyanobiphenyl (adapted from Ref. [5]) and (b) chemical 'phase diagram' built for a tetracatenar-2,2′-bipyridine (adapted from Ref. [9]). Cr = crystal, N = nematic, S_A = smectic A, S_c = smectic C, Cub = cubic, Col_h = columnar hexagonal and I = isotropic liquid. 1 MPa = 9.87 at.

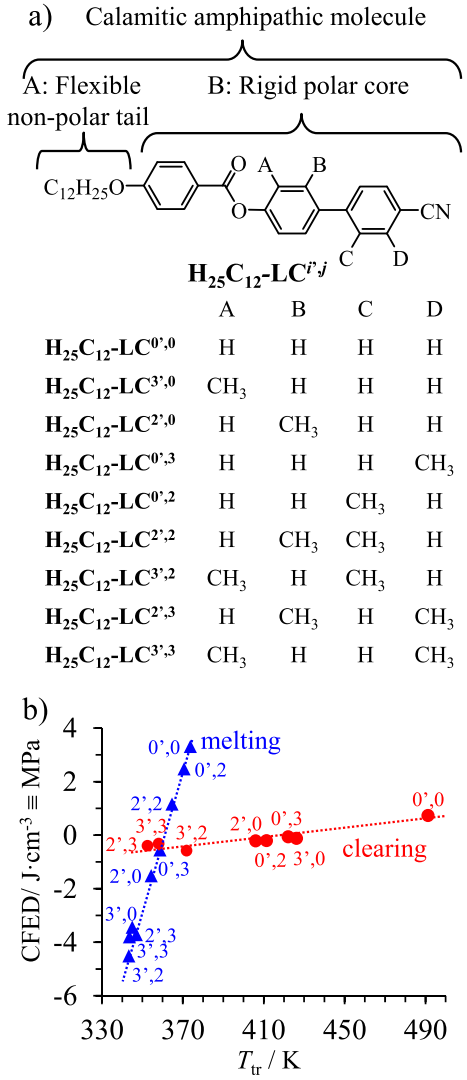

	A	B	C	D
$H_{25}C_{12}$-LC$^{0',0}$	H	H	H	H
$H_{25}C_{12}$-LC$^{3',0}$	CH_3	H	H	H
$H_{25}C_{12}$-LC$^{2',0}$	H	CH_3	H	H
$H_{25}C_{12}$-LC$^{0',3}$	H	H	H	CH_3
$H_{25}C_{12}$-LC$^{0',2}$	H	H	CH_3	H
$H_{25}C_{12}$-LC$^{2',2}$	H	CH_3	CH_3	H
$H_{25}C_{12}$-LC$^{3',2}$	CH_3	H	CH_3	H
$H_{25}C_{12}$-LC$^{2',3}$	H	CH_3	H	CH_3
$H_{25}C_{12}$-LC$^{3',3}$	CH_3	H	H	CH_3

Fig. 2. (a) Chemical structures of substituted amphipathic cyanobiphenyls $H_{25}C_{12}$-LC$^{i',j}$ and b) cohesive Gibbs free energy densities $CFED_{cryst}$ *versus* melting temperature T_m (blue triangles, T_{ref} = 360.6 K) and $CFED_{liq\text{-}cryst}$ *versus* clearing temperatures $T_{clearing}$ (red disks, T_{ref} = 443.4 K). Units: 1.0 J·cm^{-3} = 1.0 MPa. Redrawn from Ref. [20].

(odd/even) of methylene rotors [8c]. Thanks to their impressive synthetic capabilities, chemists exploited this method to inspect a large number of small perturbations affecting the phase transitions, for which it would have been at least time-consuming, but probably impossible within the frame of realistic human efforts, to record standard *P-T* phase diagrams for each isolated compound. Consequently, the intuitive short-cut highlighted in Fig. 1b is well accepted in the chemical community and, even if no theoretical support is available, qualitative structural parameters estimating the magnitude of the chemical perturbations are regularly taken as valuable estimations for 'pressure increments' when building chemical pseudo-phase diagrams. Inspired by the classical theories of entropically-driven hard-rod models [10] combined with the statistical treatments of long-range enthalpic contributions responsible for the attractive intermolecular potentials operating between interacting molecules in liquid crystals [11], Skoulios and Guillon tried to reconcile classical thermodynamics with these intuitive 'chemical pseudo-phase diagrams' [12]. These authors suggested that the formation of a thermotropic mesophase, i.e. a phase produced by the melting of the solid (referred to as the melting process in liquid crystals), but separated from the isotropic liquid by a second melting process (referred to as the clearing process

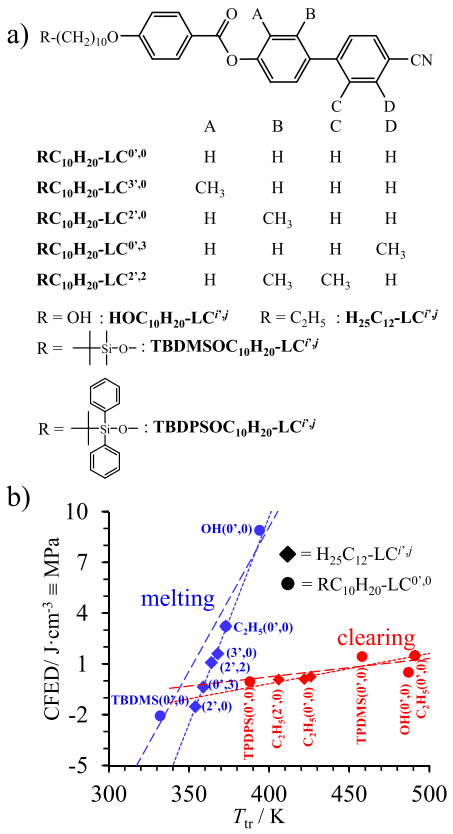

Fig. 3. (a) Chemical structures of substituted cyanobiphenyls $\mathbf{RC_{10}H_{20}\text{-}LC^{i',j}}$ and b) cohesive Gibbs free energy densities $CFED_{cryst}$ *versus* melting temperature T_m (blue markers) and $CFED_{liq\text{-}cryst}$ *versus* clearing temperatures $T_{clearing}$ (red markers) [20]. Units: 1.0 J·cm^{-3} = 1.0 MPa. Dashed traces correspond to boundaries obtained by varying R groups, whereas dotted traces are used for boundaries obtained by varying ***i'j*** substituents.

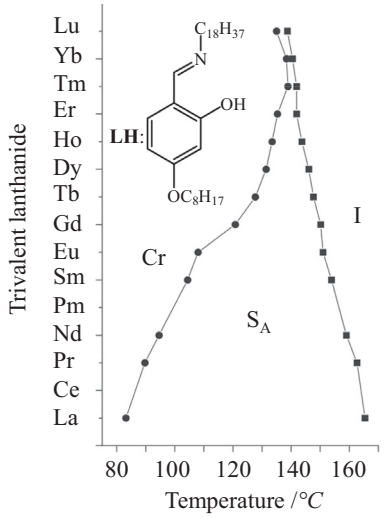

Fig. 5. Influence of the lanthanide ion on the transition temperatures for the complexes $[Ln(LH)_3(NO_3)_3]$, the structure of which is shown in Fig. 4a [38]. Cr = crystal, S_A = smectic A, I = isotropic liquid. Redrawn from Ref. [33b].

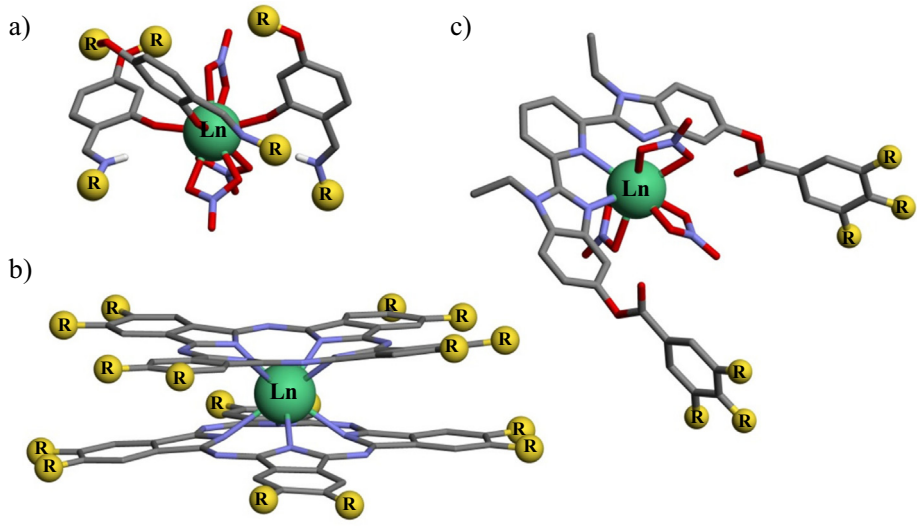

Fig. 4. Chemical structures of selected lanthanidomesogens inducing (a) calamitic (smectic A) [34], (b) discotic (columnar hexagonal) [35] and (c) cubic (bicontinuous) [36] thermotropic mesophases. Color codes: Ln = green, C = gray, N = blue, O = red, R = long linear alkoxy or alkyl chains are represented with yellow spheres.

in liquid crystals) arose when the molecules under investigation possessed two incompatible parts. Such amphipathic molecules, which should not be restricted to solely amphiphilic systems [13], are usually constituted of long, flexible and poorly polarizable saturated hydrocarbon chains connected to rigid, and highly polarizable polyaromatic cores [14]. Simplistically, the minimum energy in the macroscopic crystalline phase corresponds to a micro-segregated organization of the amphipathic molecules, which maximizes the dominant intermolecular multipolar electrostatic interactions between the polarizable aromatic cores, while the 'frozen' full extended hydrocarbon chains fill the voids. Upon increasing the temperature, a dominant entropic gain results from the decorrelation of the flexible alkyl chains and, at the melting temperature T_m, the magnitude of this contribution $T_m\Delta S_m$ balances exactly the inter-chain cohesive enthalpy. With this in mind, a thermotropic mesophase generated by amphipathic molecules can be roughly thought as a state of matter made up of clusters of packed semi-organized rigid cores dispersed in a continuum of molten paraffinic chains. The enthalpic cohesive energy responsible for the supramolecular organization in the mesophase thus mainly originates from the residual intermolecular interactions between the polarizable rigid cores, a contribution which can be balanced at higher temperature, i.e. at the clearing temperature T_c, by the minor entropic gain $T_c\Delta S_c$ produced by their decorrelation in the isotropic liquid. This qualitative description was latter completed with some explicit considerations of the supramolecular intermolecular interactions at the origin of the different cohesive energies occurring in condensed phases made of amphipathic molecules [15]. This approach culminated with the planned and successful introduction of bulky metallic complexes into mesophases [16] in order to design room-temperature lanthanidomesogens, *i.e.* lanthanide-containing liquid crystals [17].

Further theoretical advances considered that the two nano-spaces produced by the incompatible components of a binary A–B amphipathic molecule are closely related to the macroscopic segregation (demixing) of two liquids with molecular structures similar to the two segments A and B forming the amphiphile (see Fig. 2a for a molecular illustration) [18]. Modeling the Gibbs free energy of mixing (ΔG_{mix}) of the A and B blocks with the help of the Huggins-Flory theory [19] leads to the emergence of the interaction parameter χ_{AB} (Eq. (2)), which measures the enthalpic adhesion between the two separated phases $\Delta H_{mix} = RT(n_A\phi_B\chi_{AB})$, where n_A is the number of mole and ϕ_B is the volume fraction of part B in the block copolymer [20].

$$\chi_{AB} \approx \frac{V_{seg}}{RT}\left[\left(\frac{\Delta H^{A}_{vap} - RT}{V^{A}_{mol}}\right)^{1/2} - \left(\frac{\Delta H^{B}_{vap} - RT}{V^{B}_{mol}}\right)^{1/2}\right]^2 = \frac{V_{seg}}{RT}\left[\left(CED^{A}\right)^{1/2} - \left(CED^{B}\right)^{1/2}\right]^2 \quad (2)$$

In Eq. (2), V_{seg} is the reference volume of a unit segment in the polymer and $CED^i = \left(\Delta H^i_{vap} - RT\right)/V^i_{mol}$ is the cohesive energy density of a pure liquid i having the same characteristics as those of the selected i component of the block copolymer where V_{mol} is the molar volume of the liquid and ΔH_{vap} is its molar enthalpy of vaporization [21]. The larger the difference between the cohesive energy densities of the two segments of the amphipathic molecule,

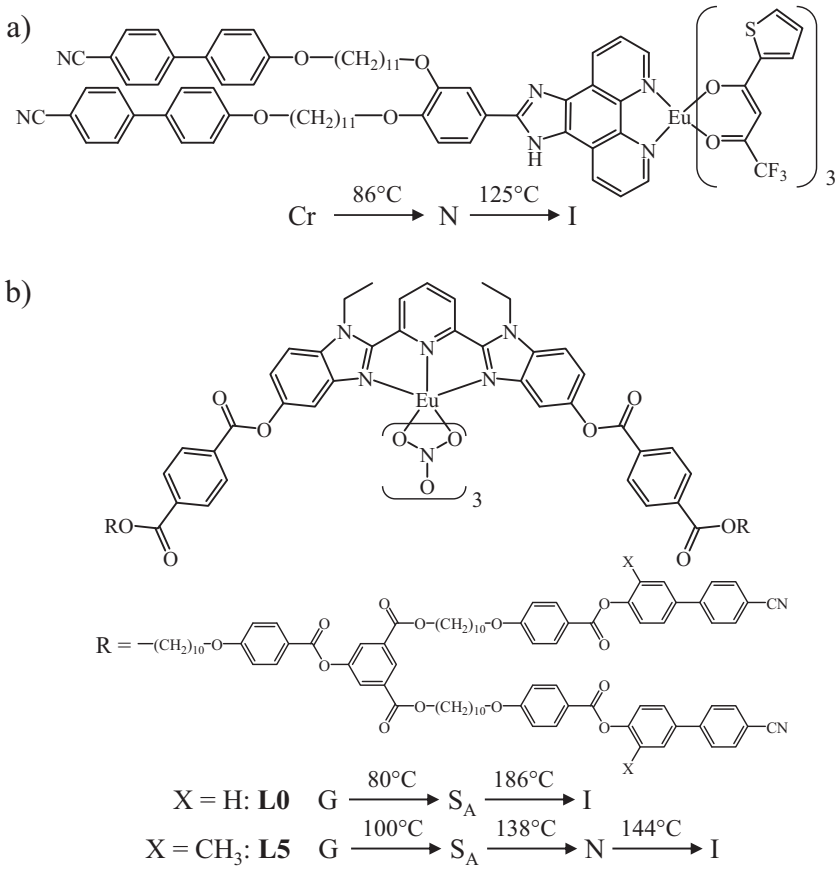

Fig. 6. Chemical structures of lanthanidomesogens exploiting mesogenic cyanobiphenyl-based dendrimers connected to a) didentate [29a and b]) tridentate [43] binding units. G = glass, Cr = crystal, S_A = smectic A, N = nematic, I = isotropic liquid.

the more positive χ_{AB} and demixing spontaneously occurs ($\Delta G_{mix} = \Delta H_{mix} - T\Delta S_{mix} > 0$) leading to microsegregation and the formation of a mesophase. When the temperature is increased to reach the clearing point (at T_c), the contribution of the mixing entropy $-T_c\Delta S_{mix}$ exactly balances the enthalpic cohesion and mixing occurs to give the isotropic liquid ($\Delta G_{mix} = 0$). We need to stress here that this scenario neglects the entropic contribution to the cohesive energy density operating in the mesophase (in Eq. (2), CED depends only on ΔH_{vap}), an hypothesis only valid for 'liquid-like' mesophases obeying the empirical Trouton's rule, which fixes a constant value of $\Delta S_{vap} = 85–88\ J\ mol^{-1}\ K^{-1}$ for the entropy of vaporization of any liquid [22]. However, the latter assumption cannot be taken for granted in solids or in liquid crystals, for which variable entropic contributions to the cohesive energy densities must be taken into account. As a consequence, the concept of cohesive energy density, only adapted to liquids (CED in Eq. (10)), is replaced by that of cohesion Gibbs free energy density (CFED in Eq. (3)), which includes both enthalpic and entropic contributions required for approaching melting (tr = m) and clearing (tr = c) processes [23].

$$\mathrm{CFED} = \frac{\Delta G^{T^{ref}}_{cohesion}}{V_{mol}} = \frac{\Delta H_{tr} - T^{ref}\Delta S_{tr}}{V_{mol}} \quad (3)$$

$\Delta G^{T^{ref}}_{cohesion}$ is the Gibbs free energy of cohesion, which estimates the degree of cohesion occurring in a condensed phase at a reference temperature T^{ref} different from the transition temperature $T_{tr} = \Delta H_{tr}/\Delta S_{tr}$ at which $\Delta G^{T_{ref}=T_{tr}}_{cohesion} = 0$. $\Delta G^{T^{ref}}_{cohesion}$, henceforth CFED, can be easily computed using Eq. (3) as soon as the enthalpy (ΔH_{tr}) and entropy (ΔS_{tr}) of transition are available at a selected reference temperature T^{ref} [23a]. Empirically, it was observed that the plot of CFED for a series of compounds submitted to chemical perturbations as a function of their transition temperatures gives a linear correlation as illustrated for the mesogenic cyanobiphenyls **$H_{25}C_{12}$-LC^{i,j}** (Fig. 2b), in which the positions and number of methyl groups is systematically varied [24]. The different slopes found for the solid-liquid phase boundary (blue triangles in Fig. 2b) and liquid crystal-liquid phase boundary (red disks in Fig. 2b) correspond to different cohesive entropy densities $S = -(\partial G/\partial T)_P$ [6] operating in the crystalline phase and in the mesophase. The latter parameter can be taken as a reporter for the sensitivity of the transition temperatures to the nature of the applied chemical perturbation: a steep slope implies a limited influence of the chemical perturbation on the transition temperature, the reverse being adequate for a gentle slope. The two different traces observed for the melting and for the clearing processes represented in Fig. 2b bring a strong and quantitative support to the original intuition of Skoulios and Guillon, which claimed that the melting and clearing processes in thermotropic liquid crystals can be separately assigned to the specific decorrelation of the flexible alkyl chains, respectively the rigid cores [12,13]. Recent theoretical work demonstrated that the CFED for a given member of the family of compounds submitted to a chemical perturbation indeed

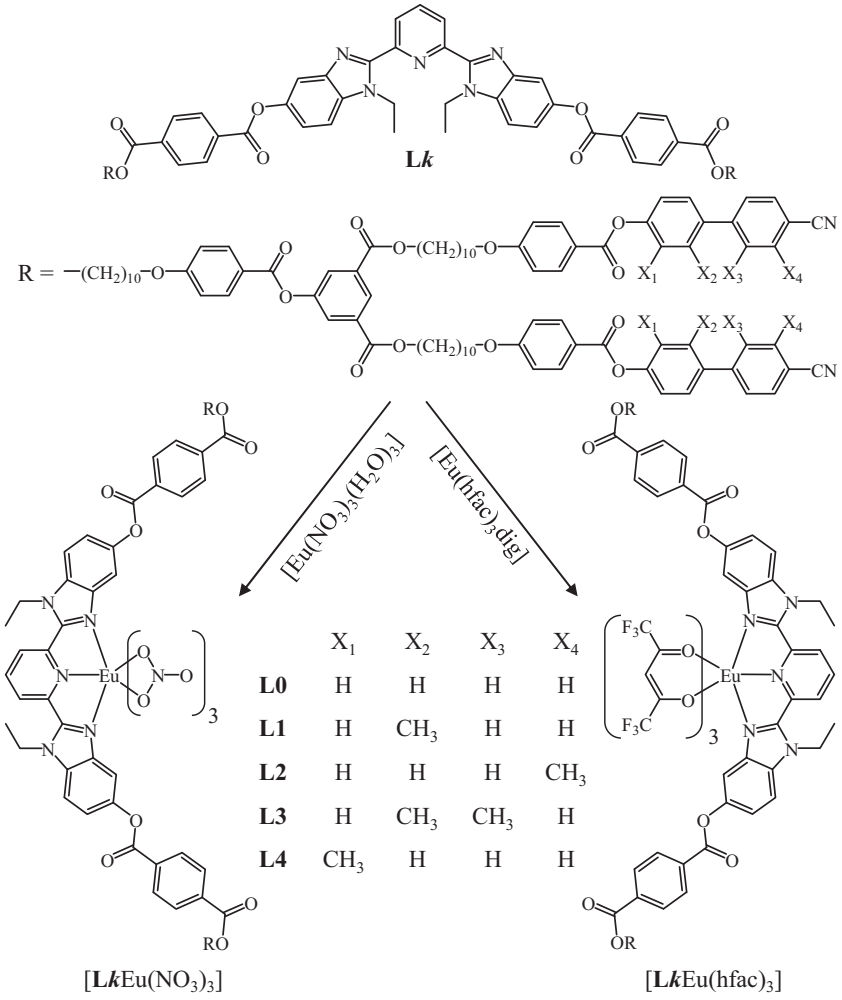

Fig. 7. Chemical structures of the dendrimeric ligands **L0–L4** and resulting lanthanidomesogens [**Lk**Eu(NO$_3$)$_3$] and [**Lk**(Eu(hfac)$_3$] (hfac = 1,1,1,5,5,5-hexafluoro-2,4-pentanedionate) investigated in this work.

reflects the 'chemical changes' or 'chemical efforts' required for shifting its specific melting temperature toward the reference temperature T_{ref} of the family, a parameter which is proportional to a pressure increment ΔP modulated by the relative molar volume expansion occurring at the transition temperature $\lambda = \Delta V_{tr}/V_{mol}$ (Eq. (4)) [20].

$$\mathrm{CFED} \approx \frac{\Delta V_{tr}}{V_{mol}}\Delta P = \lambda \Delta P \qquad (4)$$

In simpler words, the CFED *versus* T_{tr} correlations exhibited in Fig. 2b are the 'chemical equivalent' of melting and clearing boundaries found in *P-T* phase diagrams.

In a family of similar compounds exposed to minor chemical perturbations, the relative molar volume expansion λ is a constant [24] and Eq. (4) transforms the pseudo-phase diagrams usually established by chemists (Fig. 1b) into physically meaningful *P-T* phase diagrams (Fig. 2b), from which some rationalizations of the effect of chemical perturbations on the temperature-domain of existence of liquid crystals become accessible. Applied to the global modifications imposed to the cyanobiphenyls **RC$_{10}$H$_{20}$-LC$^{i',j'}$** depicted in Fig. 3a, the novel CFED *versus* T_{tr} plots built in Fig. 3b indicate that the terminal **R** groups, which disturb the packing of the flexible alkyl chains, mainly affects the melting boundary, while specific ***i'j'*** methyl substitution of the rigid core influences the clearing boundary [20].

This approach might significantly contribute to technological innovations [25], especially for 4′-cyanobiphenyl derivatives [26], which are exploited worldwide as industrial low-molecular weight liquid crystals [27] and for polymeric [28] and metal-containing [29] liquid crystals programmed with specific magnetic and optical responses. In this context, the introduction of trivalent lanthanide cations, which are well-known to exhibit predictable electronic properties [30] into thermotropic mesophases with tunable temperature domains would represent a significant and promising breakthrough. Although the embodiment of transition metal complexes into liquid-crystalline phases to generate metallomesogens was the subject, at the turn of the last century, of considerable hope for inducing novel properties and innovative applications [31], the achievement was mainly limited to the incorporation of pseudo-spherical metallic cores into molecules displaying either rod-like or disk-like anisometries, two geometries compatible with the formation of calamitic, and discotic mesophases, respectively [32]. With their large coordination numbers and variable geometries, lanthanide complexes proved to be difficult to match these criteria, but samples of the three basic types of residual organizations found in thermotropic mesophases, i.e. calamitic, discotic and cubic (Fig. 4), were reported for this class of materials during the last two decades [33]. The design of a lanthanidomesogen usually follows a synthetic strategy, in which a (pro)mesogenic ligand containing a rigid and polarizable multidentate binding site is coordinated to a bulky lanthanide cation Ln^{III} or a neutral salt LnX_3 (Fig. 4) [34–36]. In order to limit the deleterious effect of the 3D-expansion of the rigid core accompanying its complexation to the metal, the 'active binding site' is embedded within a cavity decorated with a large number of divergent flexible alkyl-type chains (Fig. 4) [37].

However, the influence of the slight contraction of the lanthanide size along the series is still detectable in the associated 'chemical pseudo-phase diagram' depicted in Fig. 5 [38], a trend which could benefit from a quantitative analysis with the help of Eq. (4). Inspired by the fruitful incorporation of pseudo-spherical bulky fullerenes [39], octasilsesquioxane [40] and ruthenium clusters [41] into thermotropic mesophases thanks to their connection to mesogenic cyanobiphenyl-based amphipathic dendrimers [42], didentate [29a] and tridentate [43] binding units were connected to related dendrimeric units and their coordination to trivalent lanthanides lead to remarkable luminescent liquid-crystalline phases (Fig. 6) [31h].

As of today, the temperature domain of existence of the latter dendrimeric lanthanidomesogens are not suited for practical applications, but the use of the cohesive free energy density concept for monitoring, in term of pressure increment (Eq. (4)), the effect of chemical perturbations on these cyanobiphenyl-based systems opens novel perspectives for rationally tuning their melting and clearing temperatures. We therefore propose here to tutorially apply Eq. (4) for the quantitative evaluation of the potential of three different chemical perturbations for programming the phase transition temperatures and the residual organization in the luminescent dendrimeric complexes [***Lk***Eu(NO$_3$)$_3$] and [***Lk***Eu(hfac)$_3$] (Fig. 7).

Reminding here that nitrate anions are known to favor intermolecular dimerization in lanthanide complexes leading to intricate mixtures [43c,44,45] whereas fluorinated acetylacetonates lead to monomers [46], we first explore, in the Section 2, the synthesis of the mesogenic dendrimeric ligands **L0**–**L3** and their subsequent complexations to the neutral lanthanide carriers [Eu(NO$_3$)$_3$] and [Eu(hfac)$_3$]. In the Section 3, the systematic methyl substitution of the aromatic cores will be exploited for tuning the melting and clearing processes in the lanthanide complexes [20,23,24]. Finally, the Section 4 is dedicated to the unique opportunity offered by dendrimeric structures to deliberately introduce controlled structural defects into lanthanidomesogens, which indeed corresponds to the prototypical case of chemical perturbations usually found in industrial polymers and liquid crystals.

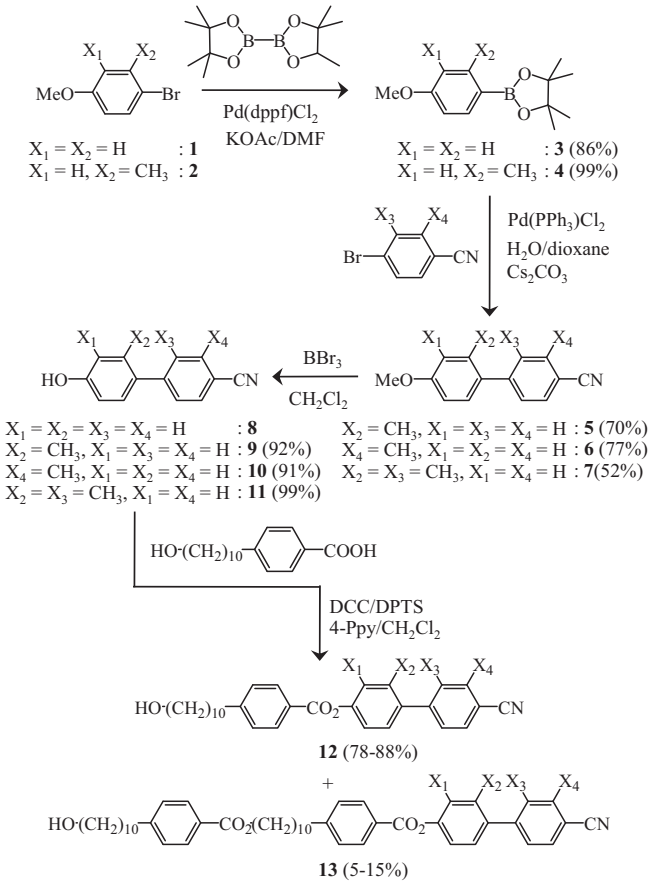

Scheme 1. Synthesis of substituted 4′-hydroxy-4-cyanobiphenyls **9**–**11** followed by polydisperse esterifications leading to mixtures of **12** and **13** (DCC = *N,N′*-dicyclohexylcarbodiimide, DPTS = 4-(dimethylaminopyridinium)-4-toluenesulfonate, 4-Ppy = 4-pyrrolidinopyridine).

2. Synthetic strategies for the preparation of luminescent dendrimeric europium complexes

The multistep strategy elaborated for ligands **L0–L3** (Fig. 7) starts with an improved Suzuki-Miyaura synthesis of substituted 4′-hydroxy-4-cyanobiphenyls **9–11**, in which boronic acids derived from **1** and **2** [23,44] have been replaced with boronic esters **3** and **4** because of their easier purifications and isolations (Scheme 1).

Esterification using 4-(10-hydroxydecyloxy)benzoic acid [39,41,44] provides the target monoester compounds **12** in good yields, together with a small amount (5–15%) of the bis-ester **13**, which results from a side reaction of **12** with an additional molecule of 4-(10-hydroxydecyloxy)benzoic acid (Scheme 1). The set of two supplementary doublets in the aromatic part of the ^{1}H NMR spectrum (Fig. 8a) can be unambiguously assigned to the [AB] spin system of the parasitic *para*-hydroxybenzoic group flanked by two alkyl chains (Fig. 8b), a phenomenon previously detected in some NMR spectra reported for the second and third generations of related cyanobiphenyl dendrimers connected to arene ruthenium metallacycles [41b].

The rational exploitation of this dispersion process as a controlled source of chemical perturbation is addressed in the Section 4, but the preparation of monodisperse dendrimeric ligands **L0–L3** requires the selective protection of the terminal hydroxy group of the benzoic acid with *tert*-butyl-dimethylsilane in compound **17** (Scheme 2 and Scheme A1 and 2 in Appendix 1, Supporting Information). Its connection to the pertinent cyanobiphenyls gives the monodisperse synthons **18–21** (Fig. 8c), which finally lead to the synthesis of **L0–L3** in fair yields according to a recurrent esterification/deprotection multistep strategy (Scheme 2 and Schemes A1–3 to A1–5 in Appendix 1, Supporting information).

The mixing of stoichiometric amounts of ***Lk*** (***Lk*** = **L0–L3**) with either $Eu(NO_3)_3{\cdot}3H_2O$ in an acetonitrile/chloroform (1:1) solvent mixture or $Eu(hfac)_3$·diglyme in dichloromethane quantitatively yields to the formation of the dendrimeric complexes [***Lk***Eu$(NO_3)_3$] and [***Lk***$(Eu(hfac)_3]$, which are isolated by precipitation into cold hexane. The elemental analyses are satisfying for both ligands and complexes, but suggest some solvent contaminations, which account for 2–9% of the total weight (water, CH_2Cl_2, hexane, Table S1, Supporting Information). Thermogravimetric analysis (Figs. S1–S3, Supporting information) confirm the presence of minor solvent contents in these compounds, which are lost after isotropization (see Section 3). Following solvent loss, the ligands **L0–L3** decompose at 300 °C (573 K) and the associated complexes at 200 °C (473 K). The ^{1}H NMR spectra recorded in CD_2Cl_2 show that the average twofold symmetry characterizing the ligand strand in solution (Fig. 9a) is retained in the europium complexes (Fig. 9b and c). The considerable paramagnetic shifts observed for the signals of the protons connected to the tridentate binding units in the complexes confirm their close location to the trivalent Eu(III) cation (Fig. 9). One immediately notices that the well-established dimerization equilibria characteristics for the formation of nitrato complexes $[(\mathbf{Lk})_2Eu_2(NO_3)_6]$ (Eq. (5) in Scheme 3 and Fig. 9c) [44,45], is removed for perfluoroacetylacetonato complexes [***Lk***

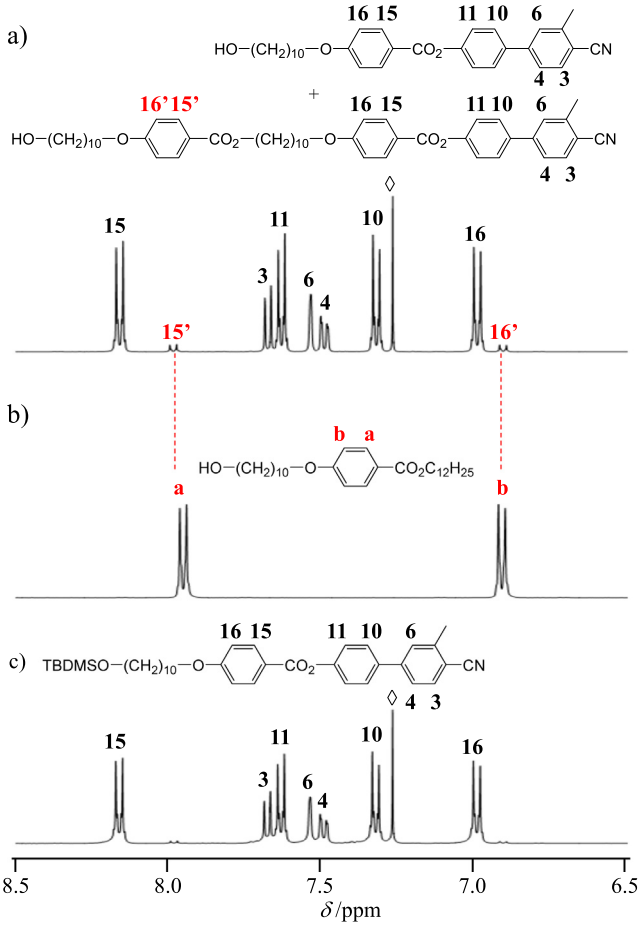

Fig. 8. Aromatic domain of the ^{1}H NMR spectra with numbering scheme showing a) polydispersity in the monoester **12** (black numbering) contaminated with the diester **13** (red numbering), b) a reference [AB] spin system modelling the parisitic para-hydroxybenzoic ester unit and c) monodispersity in the protected monoester **20**. (◊ indicates the residual signal of $CHCl_3$).

(Eu(hfac)$_3$], which are present as pure monomers in solution (Fig. 9b).

For a reference molar concentration in the standard state of $c^{\theta} = 1.0\ \text{mol}\cdot\text{dm}^{-3}$ [47], the integration of the signals extracted from variable-temperature ^{1}H NMR spectra recorded in CD_2Cl_2 (Fig. S4, Supporting Information) provides the thermodynamic constants for dimerization $K_{\text{dim}}^{\text{Eu,}\mathbf{Lk}} = |[(\mathbf{Lk})_2\text{Eu}_2]|/|[\mathbf{Lk}\text{Eu}]|^2$, from which the free energy changes $\Delta G_{\text{dim}}^{\text{Eu,}\mathbf{Lk}}$ are estimated using $\Delta G_{\text{dim}}^{\text{Eu,}\mathbf{Lk}} = -RT\ln\left(K_{\text{dim}}^{\text{Eu,}\mathbf{Lk}}\right)$. Van't Hoff plots of $-R\ln\left(K_{\text{dim}}^{\text{Eu,}\mathbf{Lk}}\right)$ *versus* T^{-1} yield straight lines (Fig. S5, Supporting Information), from which the favorable enthalpic $\Delta H_{\text{dim}}^{\text{Eu,}\mathbf{Lk}}$ and limiting entropic $\Delta S_{\text{dim}}^{\text{Eu,}\mathbf{Lk}}$ contributions to the dimerization processes can be deduced (Table 1).

When plotted together, the four van't Hoff plots intersect in close proximity of one common point with the coordinates $x = T_{\text{comp}} = 310(25)$ K (referred to as the *compensation temperature*) and $y = \Delta G_{\text{comp}} = -8.0(2.4)\ \text{kJ}\cdot\text{mol}^{-1}$ (referred to as the *compensation free energy change*) [48]. In other words, the enthalpy and entropy contributions to the dimerization processes occurring for [**Lk**Eu(NO$_3$)$_3$] (**Lk** = **L0**–**L3**) are linearly correlated and subscribe to the *H*/*S* dependence previously reported for related nitrato complexes coordinated to dendrimeric ligands of lower generations (**Lk** = **L4**–**L12** in Fig. 10) [44].

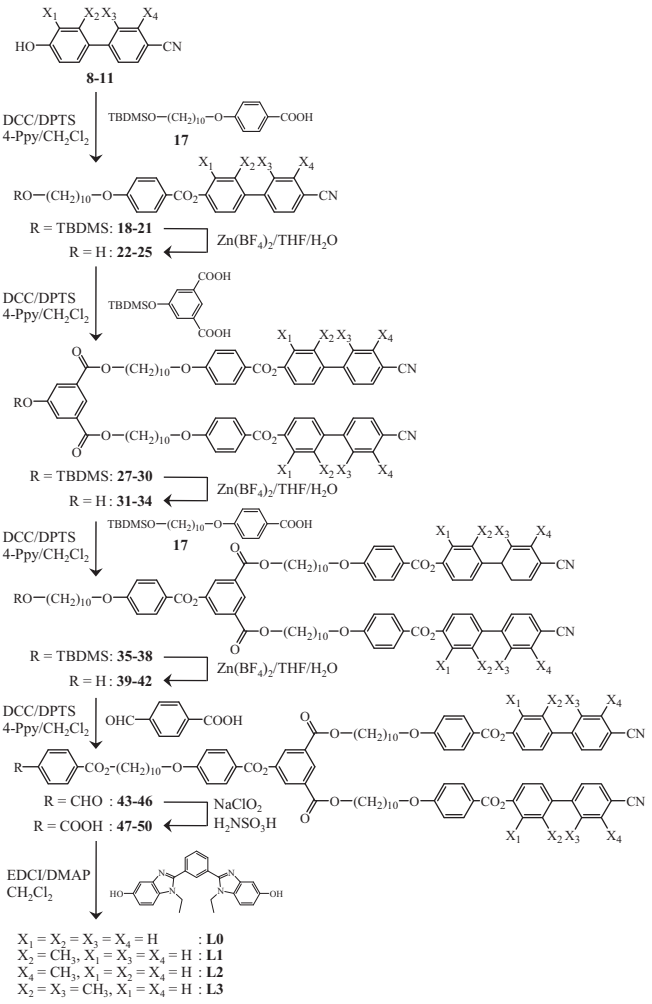

Scheme 2. Synthesis of monodisperse dendrimeric ligands **L0**–**L3** (DCC = *N*,*N*′-dicyclohexylcarbodiimide, DPTS = 4-(dimethylaminopyridinium)-4-toluenesulfonate, 4-Ppy = 4-pyrrolidinopyridine, DMAP = 4-dimethylaminopyridine, EDCI = *N*-(3-dimethylaminopropyl)-*N*′-ethylcarbodiimide).

The considerable negative cohesive enthalpies observed for the dimerization of [**Lk**Eu(NO$_3$)$_3$] complexes with the largest dendrimeric ligands **Lk** = **L0**–**L4** (red diamonds in Fig. 10) imply some stronger intermolecular interactions, but the slope (i.e. T_{comp}) of the *H*/*S* correlation is unique for the complete family. Since the latter parameter is proportional to $(r_0)^2\kappa_0$, where r_0 is the average closest distance of contact between the monomers in the dimer and κ_0 is the global force constant of the non-directional associative bond [49], we conclude that any gain in the global force constant produced by the larger number of polarizable groups involved in the dimerization of [**Lk**Eu(NO$_3$)$_3$] is accompanied by a shortening of the minimum contact distance between the two monomers.

Submitted to ultra-violet irradiations (λ_{exc} = 350–380 nm), the energy of which is compatible with the sensitization of the ligand-centered $^1\pi^*$ excited state (Fig. S6, Supporting Information), all complexes [**Lk**Eu(NO$_3$)$_3$] and [**Lk**(Eu(hfac)$_3$] (**Lk** = **L0**–**L3**) exhibit efficient light-downshifting, which eventually leads to Eu-centered emission bands (Fig. 11 and Figs. S7–S10) originating from either Eu(^{5}D$_1$) (weak green emission dominated by the $^5D_1 \rightarrow {}^7F_1$ transitions with decay lifetimes in the microsecond range, Table 2 column 2) or Eu(^{5}D$_0$) (strong red emission dominated by the $^5D_0 \rightarrow {}^7F_2$ transitions with decay lifetimes in the millisecond range, Table 2 column 4).

High-resolution emission spectra recorded in the domain of the non-degenerated Eu($^5D_0 \rightarrow {}^7F_0$) transition show one symmetrical band for each [**Lk**Eu(hfac)$_3$] complex in agreement with the existence of a single metallic environment in the solid state (Fig. 11a and Figs. S11a–S12a). For the nitrato complexes [**Lk**Eu(NO$_3$)$_3$], two different metallic sites contribute to the profile of each Eu ($^5D_0 \rightarrow {}^7F_0$) transition (Fig. 11b and Figs. S11b–S12b), which is diagnostic for the existence of mixtures of different complexes in the solid sample. In line with the thermodynamic equilibrium (5) occurring in solution, we suspect that the precipitation with hexane 'freezes' the speciation and results in mixtures of 9-coordinate monomers (EuN_3O_6 with one neutral tridentate nitrogen donor ligand and three didentate nitrate anions, see left part of Scheme 3) and 10-coordinate dimers (EuN_3O_7 with one neutral tridentate nitrogen donor ligand, three didentate nitrate anions and one additional oxygen atom from a bridging nitrate, see right part of Scheme 3). Since the energy of the main component of the Eu($^5D_0 \rightarrow {}^7F_0$) transition in [**Lk**Eu(NO$_3$)$_3$] ($\tilde{\nu}_{\text{Eu}}^{0-0} = 17{,}270\ \text{cm}^{-1}$ at 298 K, Fig. 11b) matches that found for [**Lk**Eu(hfac)$_3$] ($\tilde{\nu}_{\text{Eu}}^{0-0} = 17{,}270\ \text{cm}^{-1}$ at 298 K, Fig. 11a), for which 9-coordinate EuN_3O_6 monomeric complexation is well-established [46], the second component occurring at lower energy for [**Lk**Eu(NO$_3$)$_3$] ($\tilde{\nu}_{\text{Eu}}^{0-0} = 17{,}250\ \text{cm}^{-1}$ at 298 K, Fig. 11b) is tentatively assigned to the 10-coordinate dimer in agreement with the expected increase in nephelauxetic effect [51]. Upon pulsed excitation at 355 nm, the decay relaxation profiles of the green luminescence signals originating from the Eu($^5D_1$) excited state are monoexponential with microsecond characteristic lifetimes (Table 2, column 2). Interestingly the related red luminescence signal from Eu(^{5}D$_0$) is composed of two opposite exponential contributions showing a short rising lifetime within the microsecond domain (Table 2, column 3), which roughly mirrors the relaxation of Eu($^5D_1$), and a longer relaxation decay within the millisecond range (Table 2, column 4). These dynamic characteristics are compatible with the Jablonski diagram in Fig. 12.

With the naked eye, one can notice that the strong red luminescence obtained upon UV irradiation of solid samples is brighter for [(**Lk**)Eu(hfac)$_3$] than for [(**Lk**)Eu(NO$_3$)$_3$]. This qualitative observation is substantiated by measurements of the global absolute quantum yields $\Phi_{\text{Eu}}^{\text{L}}$ (upon excitation of the ligand excited states and monitoring the Eu^{3+} emission), which systematically increases by

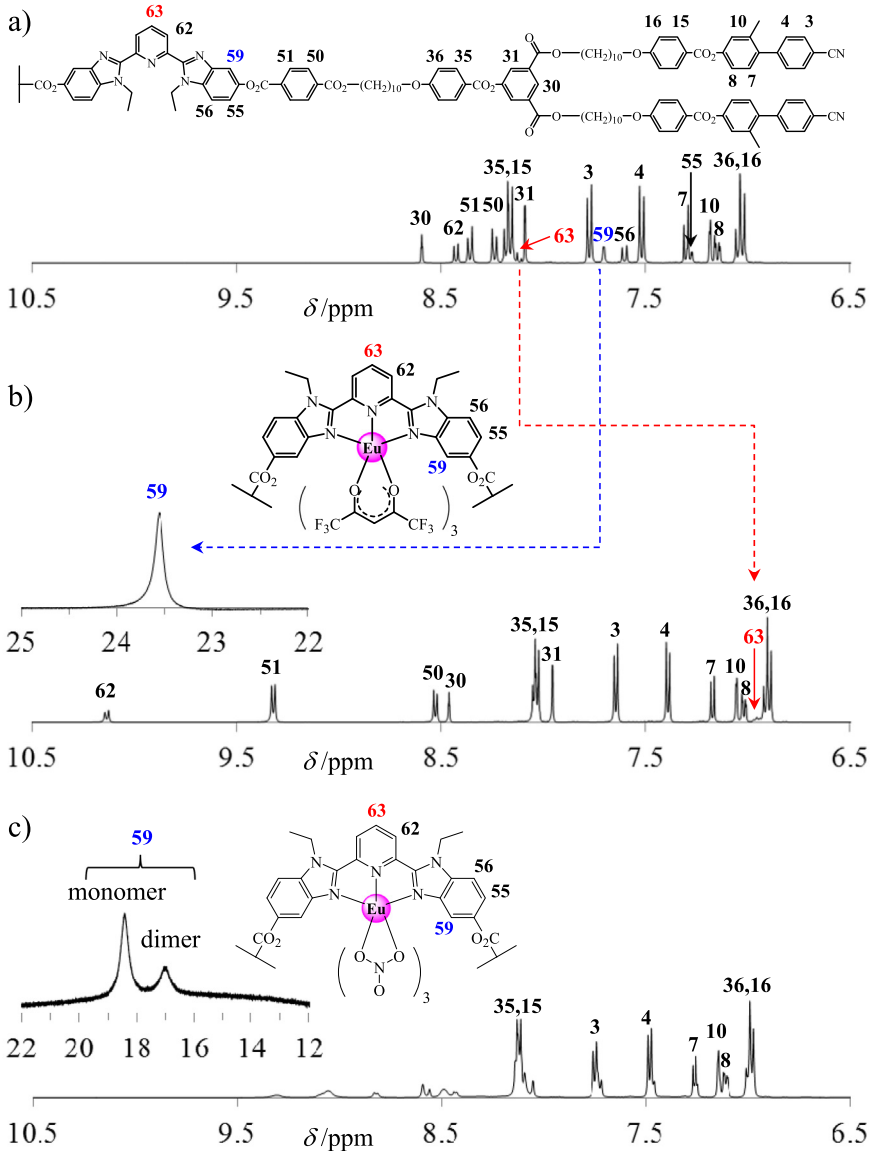

Fig. 9. Selected parts of the ^{1}H NMR spectra of a) ligand **L1**, b) complex [**L1**Eu(hfac)$_3$] and c) complex [**L1**Eu(NO$_3$)$_3$] (CD_2Cl_2, 298 K).

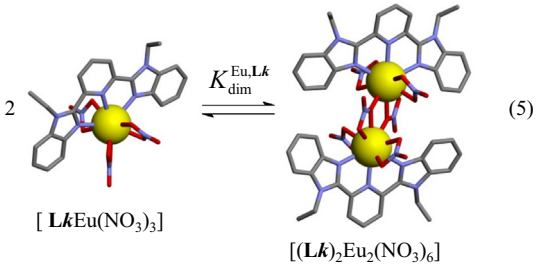

(5)

Scheme 3. Thermodynamic equilibria (Eq. (5)) previously established for the dimerization of [**Lk**Eu(NO$_3$)$_3$] [44,45]. The molecular structures are those obtained by X-ray diffraction for analogous nitrato complexes lacking in dendrimeric residues [36].

a factor of 2 in going from the nitrato to the corresponding hexafluoroacetylacetonato complexes (Table 2, column 6). Using Einstein's result for the spontaneous radiative emission rate [52], $A_{MD,0} = 14.65\ s^{-1}$ can be computed for the magnetic dipolar Eu ($^5D_0 \rightarrow {}^7F_1$) transition. Taking this value as an internal reference because of its minor dependence on the crystal-field parameters, the radiative relaxation rate constants $k_r^{Eu(^5D_0)} = \left(\tau_r^{Eu(^5D_0)}\right)^{-1}$ of the Eu($^5D_0$) level of any europium complex can be estimated with Eq. (6), where n is the refractive index of the solid, and I_{tot}/I_{MD} is the ratio between the total integrated emission arising from the Eu($^5D_0$) level to the ^7F_J manifold and the integrated intensity of the magnetic dipolar Eu($^5D_0 \rightarrow {}^7F_1$) transition [53].

$$k_r^{Eu(^5D_0)} = A(\psi_J, \psi_{J'}) = A_{MD,0} \cdot n^3 \cdot (I_{tot}/I_{MD}) \quad (6)$$

The integration of the corrected luminescence spectra recorded for [**Lk**Eu(hfac)$_3$] and [**Lk**Eu(NO$_3$)$_3$] provides radiative Eu($^5D_0$) lifetimes twice longer than the observed decay lifetimes (Table 2, column 6), thus leading to intrinsic quantum yields $Q_{Eu}^{Eu} = \tau_{obs,decay}^{Eu(^5D_0)}/\tau_r^{Eu(^5D_0)}$ close to 50% for all studied complexes (Table 2, column 7). The twofold improvement of the global quantum yields found for [**Lk**Eu(hfac)$_3$] thus results from a better sensitization efficiency $\eta_{sens} = Q_{Eu}^{Lk}/Q_{Eu}^{Eu}$ (Table 2, column 8), a parameter

Table 1
Thermodynamic Parameters for Equilibrium (5) for complexes [**Lk**Eu(NO$_3$)$_3$] (**Lk** = **L0**–**L3** in CD_2Cl_2.[a]

Complexes	$\Delta H_{dim}^{Eu,Lk}$/kJ·mol^{-1}	$\Delta S_{dim}^{Eu,Lk}$/J·mol^{-1}·K^{-1}	$\Delta G°_{dim}^{Eu,Lk}$[b]/kJ·mol^{-1})	$T_{dim,50\%}^{Eu,Lk}$[c]/K
[**L0**Eu(NO$_3$)$_3$]	−47.6(2.6)	−130.4(9.8)	−8.8(2.6)	266(25)
[**L1**Eu(NO$_3$)$_3$]	−42.2(1.8)	−105.2(6.7)	−10.9(1.8)	275(21)
[**L2**Eu(NO$_3$)$_3$]	−25.6(1.5)	−56.7(5.6)	−8.7(1.5)	244(28)
[**L3**Eu(NO$_3$)$_3$]	−31.2(1.0)	−77.2(3.8)	−8.2(1.0)	249(15)

[a] The estimated standard deviations for $\Delta H_{dim}^{Eu,Lk}$ and $\Delta S_{dim}^{Eu,Lk}$ were obtained from linear least-squares fits while those for $\Delta G°_{dim}^{Eu,Lk}$ and $T_{dim,50\%}^{Eu,Lk}$ were computed by taking into account the interdependence of $\Delta H_{dim}^{Eu,Lk}$ and $\Delta S_{dim}^{Eu,Lk}$ given by the covariance matrices.

[b] The standard free energies of dimerization were calculated at 298 K.

[c] $T_{dim,50\%}^{Ln,Lk} = \Delta H_{dim}^{Eu,Lk} / \left(\Delta S_{dim}^{Eu,Lk} + R \cdot \ln C_{tot}^{Lk}\right)$ is the temperature at which the monomer represents 50% of the ligand distribution in solution (calculated with a total ligand concentration of C_{tot}^{Lk} = 0.003 M used for NMR measurements).

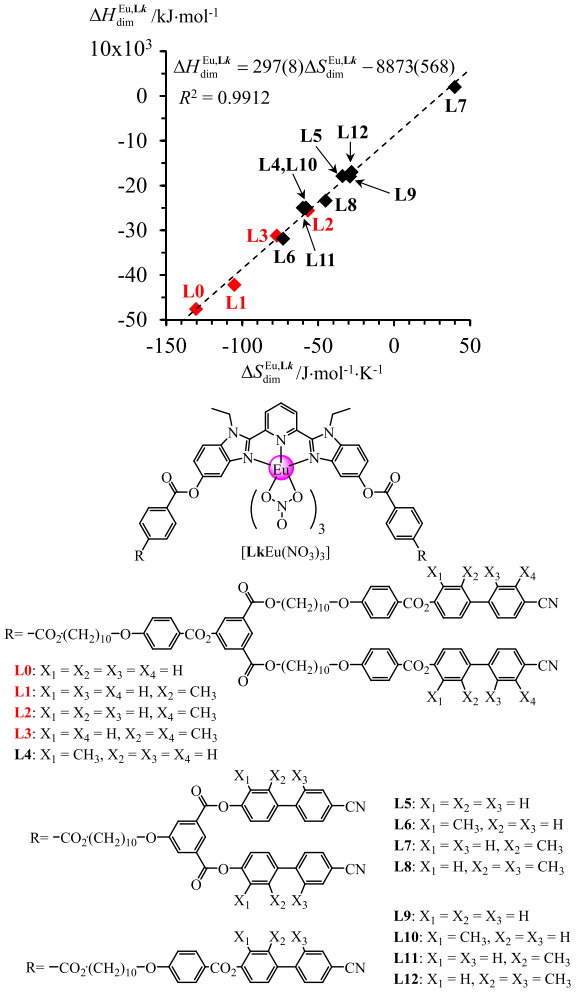

Fig. 10. Plots of enthalpy *versus* entropy values for the dimerization process modelled with Eq. (5) and occurring in CD_2Cl_2 for the complexes [**Lk**Eu(NO$_3$)$_3$] (**Lk** = **L0**–**L12**; R^2 = coefficient of determination). Red diamonds correspond to the monodisperse dendrimeric complexes reported in this contribution (**L0**–**L3**), whereas black diamonds correspond to previous data collected for smaller polydisperse dendrimeric ligands (**L4**–**L12**) [44].

which involves the efficacy of (i) the intersystem crossing $\left(k_{ISC}^{Lk}\right)$ occuring within the ligand and (ii) the energy transfer toward the europium center ($k_{EnT}^{Lk\rightarrow Eu}$, see Fig. 12). In conclusion, perfluoroacetylacetonato complexes [**Lk**Eu(hfac)$_3$] are a real improvement compared with [**Lk**Eu(NO$_3$)$_3$] for both structural aspects (pure monomers at all temperatures) and photophysical properties (higher emission quantum yield). As expected, the successive methylations of the rigid core have minor, if not negligible effects on these characteristics.

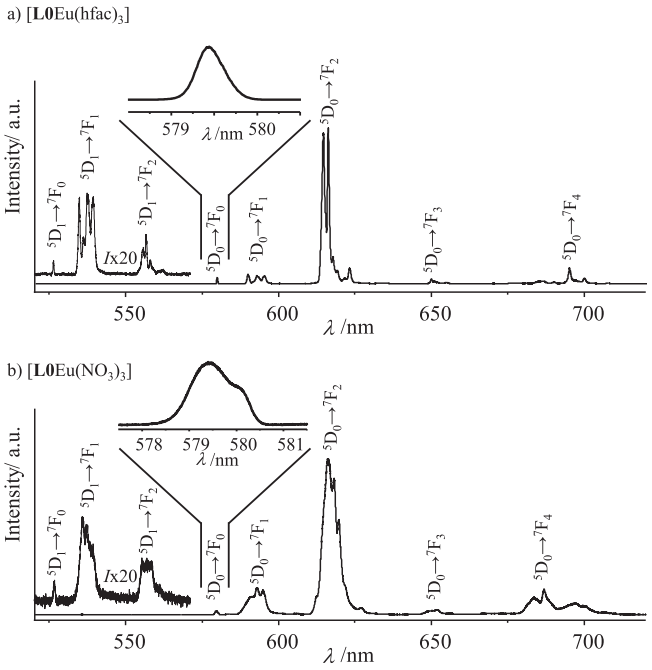

Fig. 11. Emission spectra the complexes a) [**L0**Eu(hfac)$_3$] and b) [**L0**Eu(NO$_3$)$_3$] in the solid state at 10 K (λ_{exc} = 380 nm). The 520–570 nm range showing the weak Eu ($^5D_1 \rightarrow {}^7F_j$) transitions is magnified (Intensity x20) and a high-resolution scanning of the Eu($^5D_0 \rightarrow {}^7F_0$) transition is highlighted.

3. Thermal and liquid-crystalline properties

The thermal behaviors of the ligands **L0**–**L3** and of their complexes [**Lk**Eu(hfac)$_3$] and [**Lk**Eu(NO$_3$)$_3$] were investigated by a standard combination of polarized optical microscopy (POM), differential scanning calorimetry (DSC), and low-angle X-ray scattering (LAXS) (Table 3 and Fig. 13). Upon heating the ligands **Lk** = **L0**–**L3**, the DSC thermograms display a glassy transition around 40 °C (313 K, Fig. 14a and Figs. S13a–S15a) followed by a first-order phase transition, the temperature of which regularly decreases when an increasing number of methyl groups are connected to the cyanobiphenyl cores (Fig. 13), a trend previously noticed for **RC$_{10}$H$_{20}$-LC^{i,j}** (Fig. 3) [20,24]. Typical Schlieren textures are observed by POM at temperatures between those of the two phase transitions (Fig. 14b and Figs. S13b–S15b) in agreement with the existence of a nematic organization within the mesophases (i.e. the calamitic ligands **L0**–**L3** possess no positional order, but are roughly aligned along one preferred direction). This conclusion is corroborated by variable-temperature LAXS measurements, for which no low-angle diffraction pattern could be detected in these nematic mesophases (Fig. 14c and Figs. S13c–S15c).

Rather similar DSC thermograms are recorded for the nitrato complexes [**Lk**Eu(NO$_3$)$_3$], which exhibit transition temperatures

Table 2
Europium-centered characteristic lifetimes ($\tau^{^5D_1}_{obs,decay}$, $\tau^{^5D_0}_{obs,rise}$ and $\tau^{^5D_0}_{obs,decay}$) and radiative ($\tau^{^5D_0}_{rad}$) lifetimes, intrinsic $\left(Q^{Eu}_{Eu}\right)$ and global $\left(Q^{Lk}_{Eu}\right)$ quantum yields and sensitization efficiency (η_{sens}) measured for complexes [**Lk**Eu(hfac)$_3$] and [**Lk**Eu(NO$_3$)$_3$] (**Lk** = **L0**–**L3**) in the solid state at 298 K (λ_{exc} = 355 nm).[a]

Complexes	$\tau^{^5D_1}_{obs,decay}$ /μs	$\tau^{^5D_0}_{obs,rise}$ /μs	$\tau^{^5D_0}_{obs,decay}$ /ms	Q^{Lk}_{Eu}/%	$\tau^{^5D_0}_{rad}$[b]/ms	Q^{Eu}_{Eu}[c]/%	η_{sens}[d]/%
[**L0**Eu(hfac)$_3$]	1.21(3)	1.07(4)	0.815(2)	22.9(2)	1.43(4)	57(2)	40(1)
[**L1**Eu(hfac)$_3$]	1.28(4)	1.05(5)	0.833(4)	27.4(1)	1.44(4)	58(2)	47(1)
[**L2**Eu(hfac)$_3$]	1.13(1)	1.01(3)	0.783(4)	30(1)	1.37(4)	57(2)	53(2)
[**L3**Eu(hfac)$_3$]	1.27(1)	1.05(4)	0.85(3)	23.9(4)	1.39(4)	61(3)	39(2)
[**L0**Eu(NO$_3$)$_3$]	2.62(9)	1.94(6)	0.53(2):22(2)% 1.27(1):78(2)%	13.6(4)	2.24(7)	53(2)	26(1)
[**L1**Eu(NO$_3$)$_3$]	2.60(4)	2.08(5)	0.56(2):27(3)% 1.29(6):73(3)%	15.3(3)	2.24(7)	54(3)	29(2)
[**L2**Eu(NO$_3$)$_3$]	2.29(2)	1.54(5)	0.41(3):17(2)% 1.16(2):83(2)%	9.4(2)	2.03(6)	55(2)	17(1)
[**L3**Eu(NO$_3$)$_3$]	2.69(3)	2.16(5)	0.56(2):27(2)% 1.29(2):73(2)%	13.1(2)	2.24(7)	53(2)	25(1)

[a] Values measured at 10 K are gathered in Table S2, Supporting Information.
[b] Estimated with Eq. (6).
[c] $Q^{Eu}_{Eu} = \tau^{^5D_0}_{obs,decay}/\tau^{^5D_0}_{rad}$.
[d] $\eta_{sens} = Q^{Lk}_{Eu}/Q^{Eu}_{Eu}$.

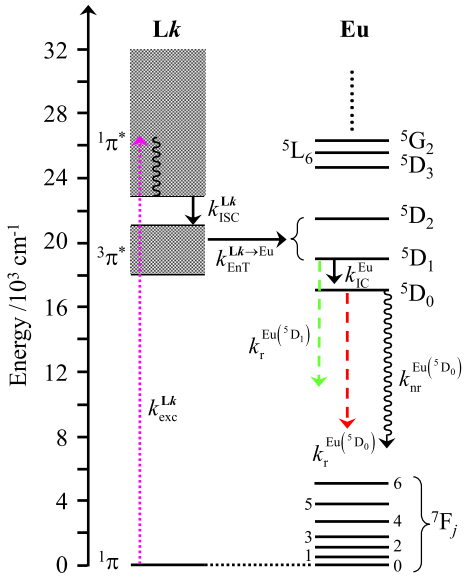

Fig. 12. Jablonski diagram for the complexes [**Lk**Eu(hfac)$_3$] and [**Lk**Eu(NO$_3$)$_3$] (**Lk** = **L0**–**L3**). The location of the excited triplet state $^3\pi^*$ centered on the tridentate binding unit was measured for a closely related complex [**L13**Gd(NO$_3$)$_3$], in which the cyanobiphenyl dendrimers were replaced by linear dodecylalkyl chains [50]. Full arrows = internal conversions, dotted arrows = excitation processes, dashed arrows = radiative relaxation processes, wavy arrows = non-radiative relaxation processes.

Table 3
Phase-transition temperatures, enthalpy and entropy changes for ligands **Lk** = **L0**–**L3**, and complexes [**Lk**Eu(hfac)$_3$] and [**Lk**Eu(NO$_3$)$_3$].

Compounds	Transitions[a]	T_{tr}/°C [K][b]	ΔH_{tr}/ kJ·mol^{-1}	ΔS_{tr}/ J·mol^{-1}·K^{-1}
L0	G → N	46 [319]		
	N → I	220 [493]	10.5(1)	21.3(2)
L1	G → N	44/ [317]		
	N → I	182 [455]	10.2(1)	22.4(2)
L2	G → N	43 [316]		
	N → I	173 [446]	8.3(1)	18.6(2)
L3	G → N	48 [321]		
	N → I	129 [402]	10.1(1)	25.1(3)
[**L0**Eu(hfac)$_3$]	G → S$_A$	37 [310]		
	S$_A$ → N	159 [432]	27.9(3)	64.6(7)
	N → I	168 [441]	13.2(1)	29.9(3)
[**L1**Eu(hfac)$_3$]	G → S$_A$	32 [305]		
	S$_A$ → I	149 [422]	58.9(4)	140(2)
[**L2**Eu(hfac)$_3$]	G → S$_A$	33 [306]		
	S$_A$ → N	132 [405]	16.9(2)	41.7(5)
	N → I	137 [414]	2.07(5)	5.0(1)
[**L3**Eu(hfac)$_3$]	G → I	57 [330]		
[**L0**Eu(NO$_3$)$_3$]	G → S$_A$	40 [313]		
	S$_A$ → I	200 [473]	13.2(1)	2.79(2)
[**L1**Eu(NO$_3$)$_3$]	G → S$_A$	34 [307]		
	S$_A$ → I	139 [412]	15.7(2)	38.1(3)
[**L2**Eu(NO$_3$)$_3$]	G → S$_A$	34 [307]		
	S$_A$ → I	141 [414]	9.8(1)	23.7(2)
[**L3**Eu(NO$_3$)$_3$]	G → I	63 [336]		

[a] S$_A$ = smectic A phase, N = nematic phase, G = glassy state, I = isotropic liquid.
[b] Transition temperatures (onset point) and glass transition temperatures (mid-point) were obtained during the second heating/cooling cycle.

similar to those of the ligands, but adopt a completely different supramolecular organizations within the mesophases, leading to the observation of focal conic fan textures by POM, which are typical of smectic A lamellar organizations (Figs. S16–S19 in the Supporting Information). The detection of two successive diffraction peaks by LAXS, indexed as d_{001} and d_{002} reflexions (Table 4, entries 1–3) confirm the formation of layers within these mesophases with a periodicity of ~106 Å, a distance which roughly matches the total length of 119 Å estimated by molecular modelling for an extended dendrimeric [**Lk**Eu(NO$_3$)$_3$] complex [43a]. Assuming an average 5% interdigitation between the layers, Fig. 15 highlights the supramolecular organization proposed for the [**Lk**Eu(NO$_3$)$_3$] complexes in their smectic A mesophases.

We however note that the dimethylation of the rigid cyanobiphenyl core in **L3** reduces the intermolecular interactions in [**L3**Eu(NO$_3$)$_3$] to such an extent that the liquid-crystalline behavior is lost, a trend mirrored for the perfluoroacetylacetonato series, in which [**L3**Eu(hfac)$_3$] displays no mesomorphism (Fig. S22). The other [**Lk**Eu(hfac)$_3$] complexes with non-methylated (**L0**) or mono-methylated (**L1**–**L2**) ligands are mesogenic with the formation of smectic A mesophases, sometimes completed with nematic mesophases before the isotropization temperatures (Fig. 13, Fig. 16 and Figs. S20–S21).

Interestingly, the low-angle diffraction pattern recorded for [**Lk**Eu(hfac)$_3$] in their smectic A mesophases display (i) four successive fine reflections indexes as d_{001} to d_{004} (Fig. 16c), where only two peaks are observed for the analogous nitrato complexes, (ii) the periodicity is reduced to ~70 Å compared to 106 Å for the nitrato complexes (Table 4, entries 4–6) and (iii) two weak, but detectable reflections are observed at higher angles (d_a = 9.3 Å and d_b = 12.2 Å in Fig. 16c, Table 4). Assuming that (a) the two additional reflections can be indexed as the d_{100} and d_{010} reflexions

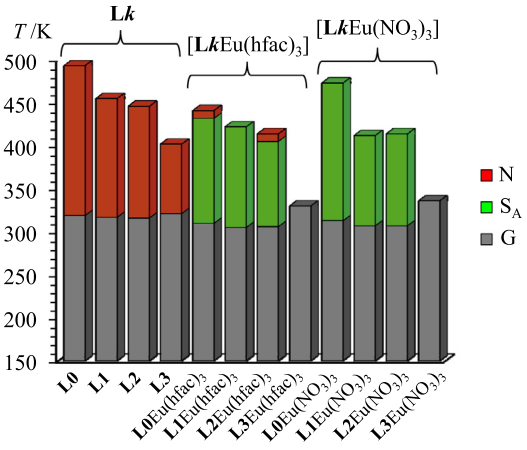

Fig. 13. Mesomorphic ranges and observed thermotropic mesophases for **Lk** = **L0**–**L3**, [**Lk**Eu(hfac)$_3$] and [**Lk**Eu(NO$_3$)$_3$] (S_A = smectic A phase, N = nematic phase, G = glassy state; scan rate 10 K/min).

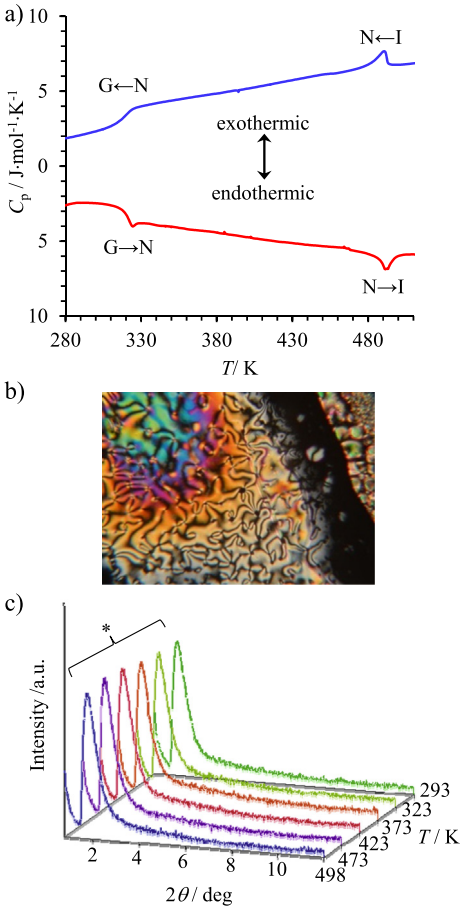

Fig. 14. Characterization of the mesomorphic properties displayed by ligand **L0**: a) DSC traces recorded at a scan rate of 10 K·min^{-1} during the second heating (red trace)/cooling (blue trace) cycle (G = glass, N = nematic, I = isotropic liquid), b) thermal optical micrograph showing Schlieren textures for the nematic phase (N) at 217 °C (490 K) and c) 3-dimensional plot of low-angle X-ray diffraction pattern recorded as a function of the temperature (λ = 1.5418 Å, * = capillary noise).

Table 4
Selected structural characteristics obtained by low-angle X-ray scattering (LAXS) for the complexes [**Lk**Eu(hfac)$_3$] and [**Lk**Eu(NO$_3$)$_3$] in their smectic A phases (λ = 1.5418 Å, **Lk** = **L0**–**L2**).

Compounds	2θ/ deg	T/K	Index/ hkl	I/a.u. [a]	d_{hkl}/Å	Unit cell [b]
[**L0**Eu(NO$_3$)$_3$]	0.81	423	001	m	110.0	
	1.62		002	w	55.0	
[**L1**Eu(NO$_3$)$_3$]	0.83	403	001	m	106.1	
	1.69		002	w	52.4	
[**L2**Eu(NO$_3$)$_3$]	0.86	403	001	m	102.9	
	1.71		002	w	51.6	
[**L0**Eu(hfac)$_3$]	1.24	423	001	s	71.3	$V \sim 8089$ Å^3
	2.51		002	m	35.5	$Z = 1$
	3.77		003	w	23.4	$\rho \sim 0.843$ g/cm^3
	5.07		004	w	17.4	
	7.23		100	w	12.2	
	9.49		010	vw	9.3	
[**L1**Eu(hfac)$_3$]	1.37	373	001	vs	64.4	$V \sim 7246$ Å^3
	2.76		002	m	32.0	$Z = 1$
	4.16		003	m	21.3	$\rho \sim 0.954$ g/cm^3
	5.53		004	w	16.0	
	7.32		100	w	12.1	
	9.56		010	vw	9.3	
[**L2**Eu(hfac)$_3$]	1.24	363	001	vs	71.3	$V \sim 8023$ Å^3
	2.49		002	m	35.5	$Z = 1$
	3.74		003	m	23.7	$\rho \sim 0.862$ g/cm^3
	4.98		004	w	17.7	
	7.29		100	w	12.1	
	9.55		010	w	9.3	

[a] s = strong, m = medium, w = weak, vw = very weak.
[b] see Appendix 2.

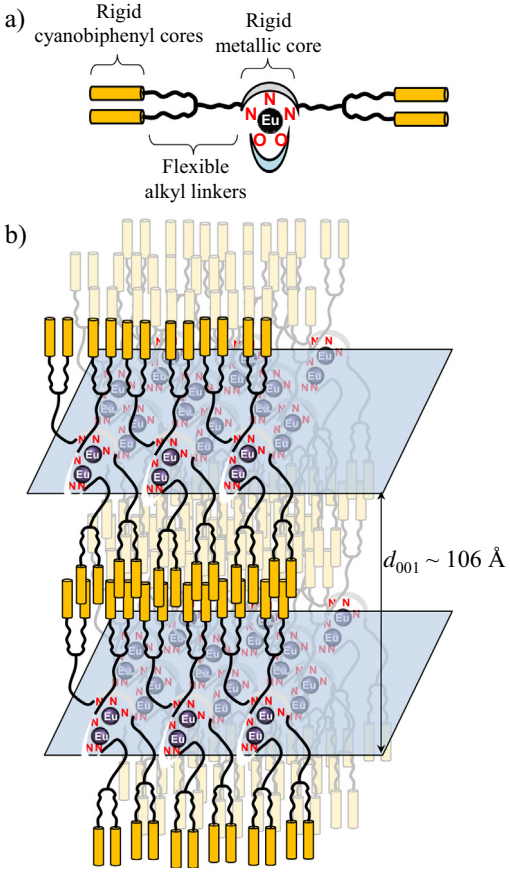

Fig. 15. a) Schematic view of dendrimeric [**Lk**Eu(NO$_3$)$_3$] complexes (**Lk** = **L0**–**L2**) and b) proposed supramolecular organization in their smectic A mesophases.

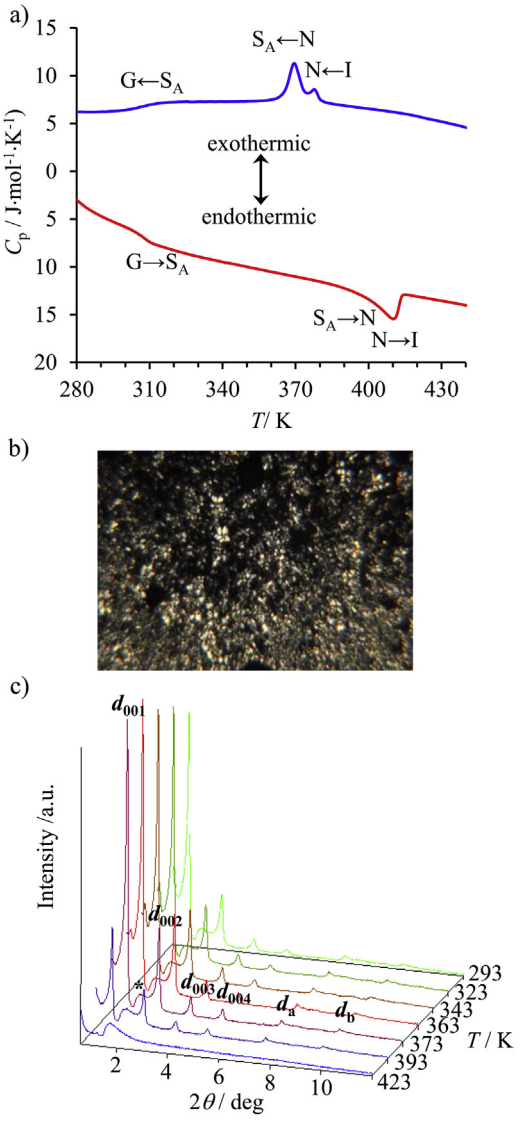

Fig. 16. Characterization of the mesomorphic properties displayed by [**L2**Eu(hfac)$_3$]: a) DSC traces recorded at a scan rate of 10 K·min^{-1} during the second heating (red trace)/cooling (blue trace) cycle (G = glass, S_A = smectic A, N = nematic, I = isotropic liquid), b) thermal optical micrograph showing focal conic fan textures in the smectic phase (S_A) at 127 °C (400 K) and c) 3-dimensional plot of low-angle X-ray diffraction pattern recorded as a function of the temperature with indexation for the 373 K (magenta) trace (λ = 1.5418 Å, * = capillary noise).

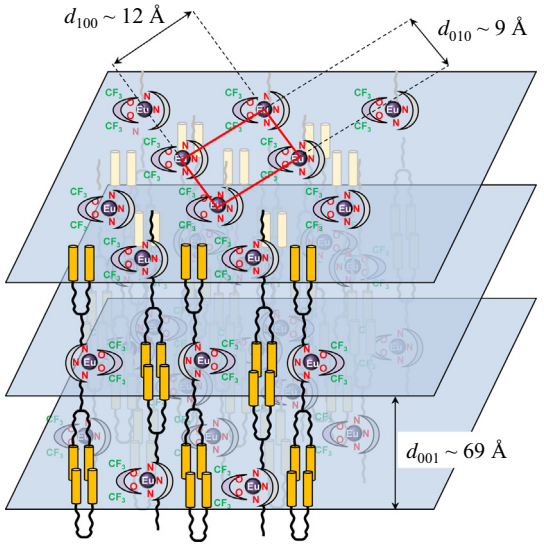

Fig. 17. Schematic view of the supramolecular organization in the smectic A mesophases of [**Lk**Eu(hfac)$_3$] complexes (**Lk** = **L0**–**L2**).

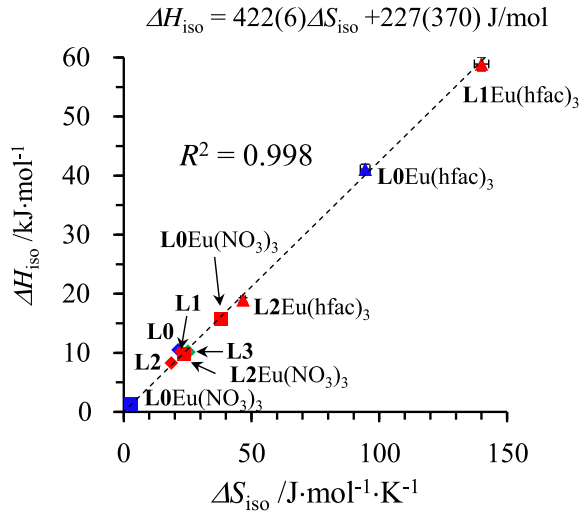

Fig. 18. Plots of enthalpy *versus* entropy values for the isotropization processes of the ligands **Lk** = **L0**–**L3** (diamonds) and of their europium complexes [**Lk**Eu(NO$_3$)$_3$] (squares) and [**Lk**Eu(hfac)$_3$] (triangles). Blue markers correspond to non-methylated cyanobiphenyls, red markers stand for mono-methylated cyanobiphenyls and green markers are used for di-methylated cyanobiphenyls (R^2 = coefficient of determination).

of a simple rectangular transverse lattice and (b) one Eu(III) center is present per unit cell ($Z = 1$), the calculated densities $0.843 \leqslant \rho \leqslant 0.954$ in the smectic A mesophases for [**Lk**Eu(hfac)$_3$] (**Lk** = **L0**–**L2**, Table 4 and Appendix 2) are compatible with $\rho \sim 1$ g·cm^{-3} expected for these class of dendrimeric metallomesogens [42,54]. With this in mind, point (i) corroborates the existence of a higher degree of organization of the dendrimeric complexes [**Lk**Eu(hfac)$_3$] within the layers in the smectic A phase (compared with [**Lk**Eu(NO$_3$)$_3$]), while point(ii) implies a much larger interdigitation (Fig. 17).

The increase in the level of supramolecular organization along the series **Lk** (nematic) ≪ [**Lk**Eu(NO$_3$)$_3$] (smectic A) ⩽ [**Lk**Eu(hfac)$_3$] (smectic A with transverse rectangular lattice) mirrors the implementation of large local transverse electric dipole moments produced by the complexation of the tridentate binding unit (Fig. S23 in the Supporting Information). The tridentate binding unit in **L0**–**L3** indeed adopts a *trans-trans* arrangement of the nitrogen atoms bearing the lone pairs, for which a weak local transverse dipole moments of only 1.7 D, mainly oriented along the C_{para}-N direction of the central pyridine ring, has been reported [55]. After coordination to [Eu(hfac)$_3$], a local dipole moment of 14.2(6) D, still roughly oriented along the C_{para}-N direction of the central pyridine ring, but pointing in the opposite direction, can be computed [55]. There is no doubt that the additional dipolar interactions improve the lateral cohesion and favor lamellar organizations in the complexes. The recurrent decrease of the isotropization temperatures observed for both ligands and europium complexes upon an increase of the number of methyl groups bound to the terminal cyanobiphenyls (i.e. T_{iso}(zero-methyl: **L0**) > T_{iso}(mono-methyl, **L1**–**L2**) > T_{iso}(dimethyl, **L3**)) can be traced back to minor changes among the intermolecular interactions mediated by the cyanobiphenyl residues as previously detailed for **H$_{25}$C$_{12}$-LC^{i,j}** (see Fig. 2) [23a]. Let's stress here that a simplistic model already predicts that the molar polarizability α_M of the

cyanobiphenyls decreases along the series α_M(no-methyl) ⩾ α_M(mono-methyl) > α_M(dimethyl), which is compatible with weaker intermolecular cohesions and lower isotropization temperatures for the methyl substituted dendrimers (Appendix 3).

Finally, the enthalpic (ΔH_{iso}) and entropic (ΔS_{iso}) contributions, which control the isotropization process occurring at $T_{iso} = \Delta H_{iso}/\Delta S_{iso}$ (Table 3, columns 4 and 5), exhibit a strict linear compensation (Fig. 18), which implies comparable changes in phase volume for all the compounds of the series [56]. The slope of the linear H/S compensation, better known as the compensation temperature [48], can be considered as an estimation for the cohesiveness existing in the mesophase following the *n*-merization process (i.e. the reverse of isotropization) [49]. For the melting processes considered here, no parasitic solvation may affect the H/S dependence [57] and the Ford-Piguet theory [49,58] predicts $T_{comp} \propto (r_0)^2\kappa_0$, where r_0 is the closest contact distance between the molecules in the (meso)phase and κ_0 is the average force constant of the non-directional intermolecular bonds [49]. Compared with the simple bimolecular dimerization occuring for $[(\mathbf{Lk})_2Eu_2(NO_3)_6]$ in dichloromethane solution (Fig. 10, T_{comp} = 297(8) K), the larger value found for the isotropization processes T_{comp} = 422(6) K points to the operation of stronger intermolecular cohesion in the mesophase probably as a result of (i) multiple intermolecular associations and (ii) the removal of competitive solvation processes in pure materials.

The concept of cohesive free energy density CFED summarized in Eq. (3) transforms the imposed chemical perturbations into pressure increments according to Eq. (4). The phase boundary CFED *versus* T_{iso} (Fig. 19) is built using a reference temperature T^{ref} = 435.6 K taken as the arithmetic mean of all considered isotropization temperatures (Table S3). One immediately notices in Fig. 19 that the two chemical perturbations investigated here, i.e. (i) successive methylation **L0** → **L1**, **L2** → **L3** and (ii) metal complexation **Lk** → [**Lk**Eu$(NO_3)_3$] or **Lk** → [**Lk**Eu(hfac)$_3$] belong to the same phase boundary within experimental errors. The associated cohesive entropy density $S_{cd} = -\partial(CFED_{iso}/V_{mol})/\partial T$ = −0.014(3) J K^{-1} cm^{-3} estimated in the mesophase at the reference temperature can be qualitatively compared with the influence of other chemical perturbations for programming transition temperatures. For instance, the stepwise increase of methylene rotors in linear alkanes has a relatively minor influence on their melting temperature (S_{cd} = −0.57(3) J K^{-1} cm^{-3}) [23], whereas the connection of an increasing amount of divergent long alkyl chains connected to polyaromatic receptors, a perturbation referred to as a polycatenar effect, strongly affects both melting (S_{cd} = −0.13 to −0.11 J K^{-1} cm^{-3}) and isotropization (S_{cd} = −0.021 to −0.013 J K^{-1} cm^{-3}) temperatures [20]. Since the CFED has pressure units, we calculate that the complexation of EuX_3 to one of the dendrimeric ligand **Lk** corresponds to a 'pressure increment' of $\Delta P_{\mathbf{Lk}\rightarrow\mathbf{Lk}Eu(NO3)3} = CFED_{\mathbf{Lk}Eu(NO3)3}$-$CFED_{\mathbf{Lk}}$ = −0.6(2) MPa for X = nitrate counter-anions and $\Delta P_{\mathbf{Lk}\rightarrow\mathbf{Lk}Eu(hfac)3} = CFED_{\mathbf{Lk}Eu(hfac)3}$-$CFED_{\mathbf{Lk}}$ = −0.9(3) MPa for X = hexafluoroacetylacetonate anions. Alternatively, the successive methylation corresponds to a pressure increment of ΔP = −0.6(2) MPa per methyl group simultaneously attached to each cyanobiphenyl termini of the dendrimeric ligand **L0**. Interestingly, these perturbations are more or less additive and we can predict that, taking ligand **L0** as a reference, the concomitant introduction of one methyl group (ΔP = −0.6 MPa) followed by its complexation to Eu(hfac)$_3$ (ΔP = −0.9 MPa) in [**L1**Eu(hfac)$_3$] or in [**L2**Eu(hfac)$_3$] is expected to produce a shift in 'chemical pressure' of $\Delta P_{tot} \sim -1.5(3)$ MPa, which roughly match the experimental data of −1.7 and −1.4 MPa experimentally observed between **L0** and these two complexes. Exploiting the pseudo-linear phase boundary built in Fig. 19, ΔP_{tot} = −1.5 MPa transforms into a temperature shift of $\Delta T_{iso} = \Delta P/(-0.014)$ = −107(23) K, which fairly matches the experimental change observed in going from **L0** to [**L1**Eu(hfac)$_3$] (ΔT_{iso} = −71 K) or to [**L2**Eu(hfac)$_3$] (ΔT_{iso} = −79 K).

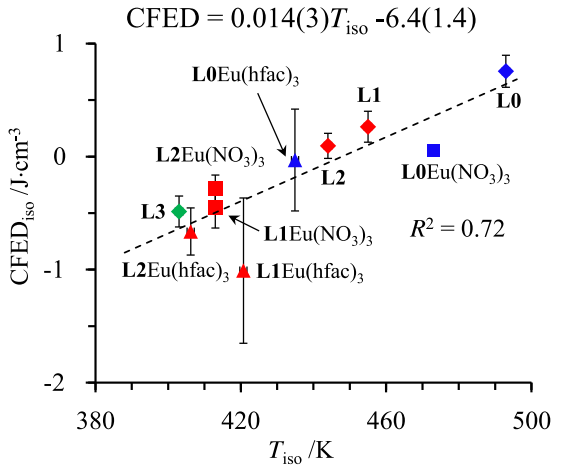

Fig. 19. Cohesive Gibbs free energy densities $CFED_{iso}$ *versus* isotropization temperature T_{iso} for the ligands **Lk** = **L0**–**L3** (diamonds) and their europium complexes [**Lk**Eu$(NO_3)_3$] (squares) and [**Lk**Eu(hfac)$_3$] (triangles) using T^{ref} = 435.6 K as the reference temperature. Blue markers stand for non-methylated cyanobiphenyls, red markers for mono-methylated cyanobiphenyls and green markers for di-methylated cyanobiphenyls (R^2 = coefficient of determination). Units: 1.0 J·cm^{-3} = 1.0 MPa.

4. Polydispersity as a pressure attenuator in phase diagrams

Since the minor perturbation induced by the methylation of cyanobiphenyl termini in the large dendrimeric ligand **L0** results in an easily detectable chemical 'pressure increment', we reasoned that the structural dispersity produced by the competitive multi-esterification of non-protected 4-(10-hydroxydecyloxy)benzoic acid (Scheme 1) may have noticeable consequences on the liquid-crystalline properties of the related polydisperse ligand poly-**L0**. If the average proportion of multi-esterification for a single reaction is set to α, the propagation of this structural defect in the final dendrimeric ligand can be predicted with the help of the binomial distribution (Scheme 4).

The synthesis of the mesogenic ligands depicted in Scheme 2 was thus repeated with non-protected 4-(10-hydroxydecyloxy) benzoic acid to give the dendrimeric ligands poly-**L0** to poly-**L2**, the polydispersity of which can be quantified by the ratio between the intensity I_{poly} of the ^{1}H NMR signals recorded for one pair of protons belonging to the [AA′BB′] spin system of the *para*-hydroxybenzoic group of the defect (red signal in Fig. 20) and the total intensity I_{tot} of two pairs of protons in two symmetrical [AA′BB′] spin systems in each oligomers (blue signal in Fig. 20).

The experimental ratio I_{poly}/I_{tot} = 0.29 (poly-**L0**), I_{poly}/I_{tot} = 0.45 (poly-**L1**) and I_{poly}/I_{tot} = 0.27 (poly-**L2**) can be fitted to Eq. (7) by using non-linear least-square methods where x_i is the mole ratio of each oligomer in the mixture (expressed as a binomial function of the average proportion of multi-esterification for a single reaction α, Scheme 4) and n_i is the number of structural defects per oligomer.

$$\frac{I_{poly}}{I_{tot}} = \frac{\sum_i 2x_i n_i}{\sum_i 4x_i} = \frac{1}{2}\sum_i x_i n_i \qquad (7)$$

The fitted average proportions of multi-esterification per coupling reaction amount to $\alpha_{\mathbf{L0}}$ = 9.7%, $\alpha_{\mathbf{L1}}$ = 15.0% and $\alpha_{\mathbf{L2}}$ = 9.0%, which allow the calculation of the distributions of the various oligomers characterized by their number average molecular weights $\bar{M}_n$, weight average molecular weights $\bar{M}_w$ and polydispersity

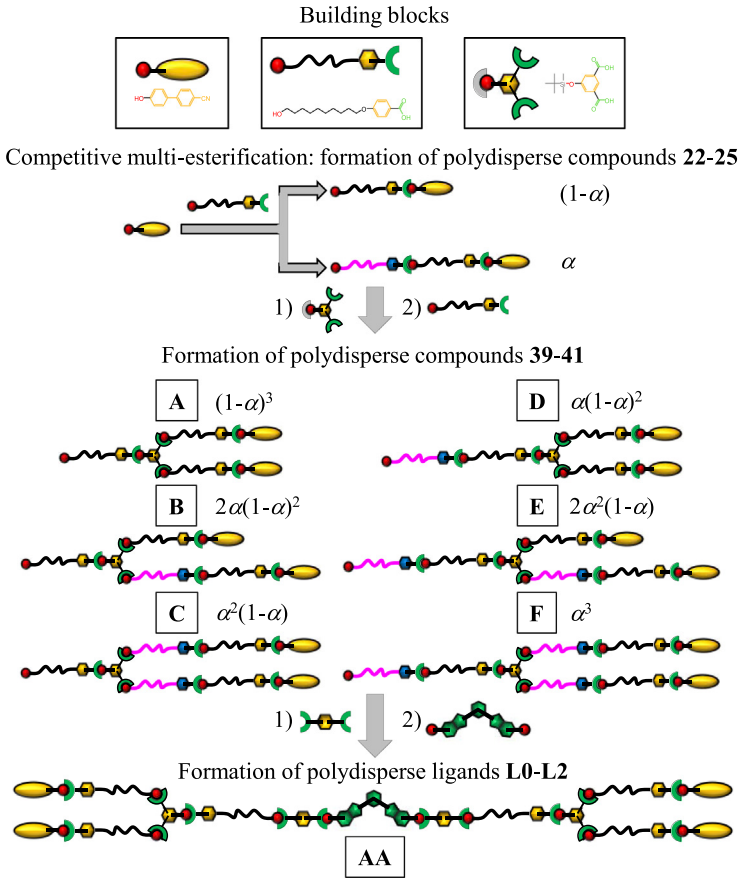

Compd	AA	AB	AC	AD	AE	AF	BB	BC	BD	BE	BF
x_i	$(1-\alpha)^6$	$(1-\alpha)^5$ 4α	$(1-\alpha)^4$ $2\alpha^2$	$(1-\alpha)^5$ 2α	$(1-\alpha)^4$ $4\alpha^2$	$(1-\alpha)^3$ $2\alpha^3$	$(1-\alpha)^4$ $4\alpha^2$	$(1-\alpha)^3$ $4\alpha^3$	$(1-\alpha)^4$ $4\alpha^2$	$(1-\alpha)^3$ $8\alpha^3$	$(1-\alpha)^2$ $4\alpha^4$
n_i	0	1	2	1	2	3	2	3	2	3	4
Compd	CC	CD	CE	CF	DD	DE	DF	EE	EF	FF	
x_i	$(1-\alpha)^2$ α^4	$(1-\alpha)^3$ $2\alpha^3$	$(1-\alpha)^2$ $4\alpha^4$	$(1-\alpha)$ $2\alpha^5$	$(1-\alpha)^4$ α^2	$(1-\alpha)^3$ $4\alpha^3$	$(1-\alpha)^2$ $2\alpha^4$	$(1-\alpha)^2$ $4\alpha^4$	$(1-\alpha)$ $4\alpha^5$	α^6	
n_i	4	3	4	5	2	3	4	4	5	6	

Scheme 4. Schematic view of the propagation of structural defects (highlighted in magenta throughout the scheme) upon competitive multi-esterification during the synthesis of poly-disperse ligand poly-**L0**–**L2**. X_i is the mole ratio of each oligomer in the mixture, n_i is the number of structural defects in each final oligomer and α is the average proportion of multi-esterification for a single reaction.

indexes $I_p = \bar{M}_w/\bar{M}_n$ (Fig. 21 and Appendix 4 in the Supporting Information). Upon reaction with Eu(hfac)$_3$·diglyme, the resulting complexes poly-[**Lk**Eu(hfac)$_3$] exhibit the same polydispersity as those found in the parent dendrimeric ligands (Fig. S24). The emission spectra obtained for poly-[**Lk**Eu(hfac)$_3$] upon ligand-centered excitation (λ_{exc} = 350 nm) in the solid state mirror those reported for the monodisperse analogues (Fig. 11a) except for a 10–18% broadening of the Eu($^5D_0 \rightarrow {}^7F_0$) transition (Fig. S25) and for some deviations from monoexponential behaviors for the Eu($^5D_0$) decays in the polydisperse samples (Table S4 in the Supporting Information). These observations suggest that the polydispersity introduces some disorder in the condensed phases, a statement confirmed by (i) the loss of clear textures observed by polarized optical microscopy in the mesophases (the observed POM micrographs are typical to those found in polymeric liquid crystals [59], Figs. S26–S27), (ii) the systematic decrease of the transition temperatures measured by differential scanning calorimetry (Fig. 22 and Table S5) and (iii) the extension of the layer periodicity measured by low-angle X-ray scattering (Appendix 5).

The plot of enthalpic *versus* entropic contributions to the isotropization processes in polydisperse compounds displays *H*/*S* compensation with a gentler slope than that found for the monodisperse analogues (Fig. 23a). According to Eq. (8) [56c], this trend can be accounted for by the existence of two different phase volume expansions $\Delta\ln(\Omega_{1,2}) = \ln(\Omega_1) - \ln(\Omega_2) = \ln(\Omega_1/\Omega_2) < 0$ accompanying the isotropization processes in the polydisperse series ($R\Delta\ln(\Omega_{1,2}^{poly}) = -3.4(1.2)\,J\,mol^{-1}\,K^{-1}$) and in the monodisperse series ($R\Delta\ln(\Omega_{1,2}^{mono}) = -1.9(1.4)\,J\,mol^{-1}\,K^{-1}$).

$$\Delta H_{iso} = T_{comp}\Delta S_{iso} - RT_{comp}\Delta\ln(\Omega_{1,2}) \quad (8)$$

When $\Delta\ln(\Omega_{1,2})$ is not a single constant along a thermodynamic *H*/*S* family, as it is the case here for mono- and poly-disperse compounds, the magnitude of $1/\Omega$ can be considered as a corrected coordinate leading to the novel extra-thermodynamic Eq. (9) (*M* is some constant characterizing the system for which $p_\Omega^2/2M$ corresponds to its kinetic energy) [56c].

$$\Delta H_{iso} = T'_{comp}[\Delta S_{iso} + R\Delta\ln(\Omega_{1,2})] - RT'_{comp}\Delta\ln(M_{1,2}) \quad (9)$$

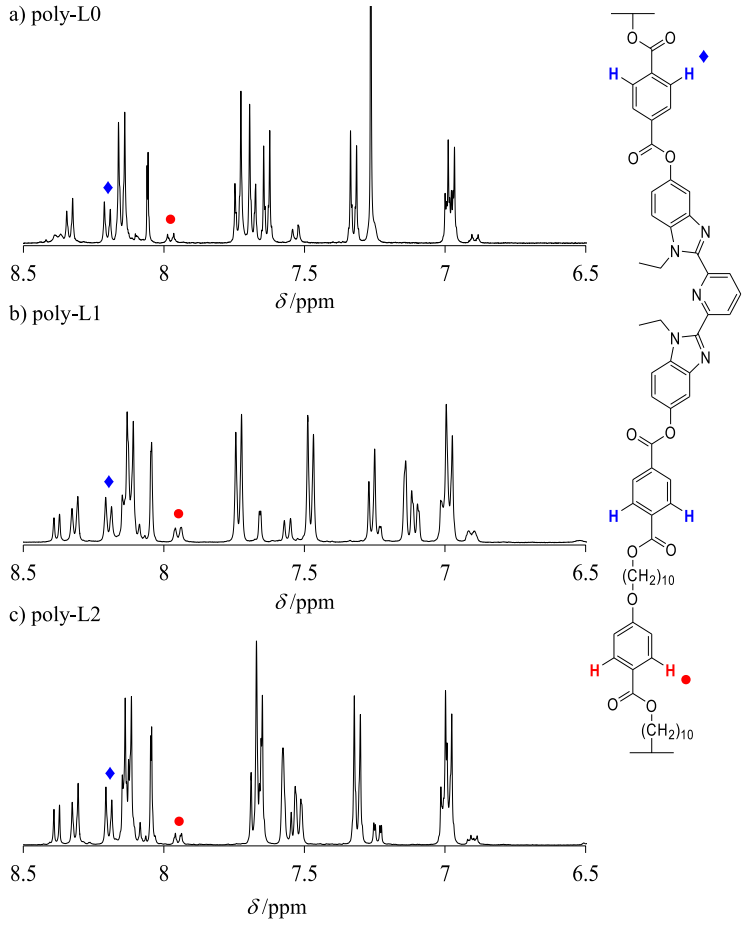

Fig. 20. Aromatic parts of the ^{1}H NMR spectra recorded for the polydisperse dendrimeric ligands poly-**L0** to poly-**L2** (CD_2Cl_2, 298 K).

The straight line observed for the corrected plot of *H versus S* $+R\Delta\ln(\Omega_{12})$ built with the help of Eq. (9) (Fig. 23b) demonstrates that (i) the constraints imposed by methyl substitution of the terminal cyanobiphenyls or by complexation of the central binding unit to [Eu(hfac)$_3$] similarly affect both series of dendrimeric ligands (i.e. monodisperse and polydisperse) leading to a unique value for *M* and (ii) the two different straight lines exemplified in Fig. 23a can be safely assigned to a simple difference in volume expansion for the two series [56c]. Finally, the plot of the cohesive Gibbs free energy densities (Table S6) as a function of the transition temperatures shows two different boundary lines possessing different slopes (Fig. 24). The gentler slope found for polydisperse samples (blue phase boundary in Fig. 24) can be assigned to a global ~30% 'attenuation' in magnitude of the pressure increments imposed by the chemical perturbations in polydisperse systems. Taking into account the expansion of the interlayer distances measured by LAXS measurements (Appendix 5), we tentatively assign this damping factor to a weaker cohesion in the polydisperse mesophases, which minimizes the consequence of the chemical perturbation in the phase diagram. It is however worth noting that, despite the reduced pressure effect, the range of transition temperatures spanned remains similar for both mono- and polydisperse series.

5. Conclusions

The mesogenic cyanobiphenyl-based amphipathic dendrimeric ligands **L0**–**L3** act as ideal scaffolds for the incorporation of luminescent lanthanide carriers [Ln(NO$_3$)$_3$] or [Ln(hfac$_3$)$_3$] into thermotropic liquid-crystalline mesophases. The already remarkable $Q^{\mathbf{Lk}}_{\mathrm{Eu,NO_3}}$ = 10–15% quantum yields measured for the conversion of UV photons into pure red emission in the nitrato complexes [**Lk**Eu(NO$_3$)$_3$] can be further extended to $Q^{\mathbf{Lk}}_{\mathrm{Eu,hfac}}$ = 25–30% in the hexafluoroacetylacetonato complexes [**Lk**Eu(hfac)$_3$]. This beneficial effect is accompanied by a simplification of the molecular speciation in solution with the exclusive formation of monomeric rod-like dendrimeric [**Lk**Eu(hfac)$_3$] complexes. Thermally-induced glassy transitions occur around 30-40 °C and lead to the formation of liquid-crystalline phases for both the ligands **L0**–**L2** and their europium complexes. Whatever the chemical perturbation imposed to the archetypal **L0** ligand (methylation of the terminal cyanobiphenyls, complexation to europium carrier, introduction of structural defects), the melting temperatures are not significantly affected, but the temperatures of the isotropization processes (T_{iso}), which transform the liquid crystals into isotropic liquids, show some unambiguous variations. Thanks to the combination of *H*/*S* compensations with phase boundaries provided by cohesive Gibbs free energy densities (CFED) *versus* T_{iso} plots, we were able to quantify the effect of chemical perturbations as 'pressure increments' applied to the system. Typically, the connection of one additional methyl per terminal cyanobiphenyls in **L0**–**L2** counts for a pressure increment comparable with the complexation process transforming **L0**–**L2** into their europium complexes. These perturbation are roughly additive, which provides a set of novel predictive tools for programming the domain of existence of liquid-crystalline phases in lanthanidomesogens. Detailed structural investigations of the supramolecular organization in the mesophases highlight the expected predominance of intermolecu-

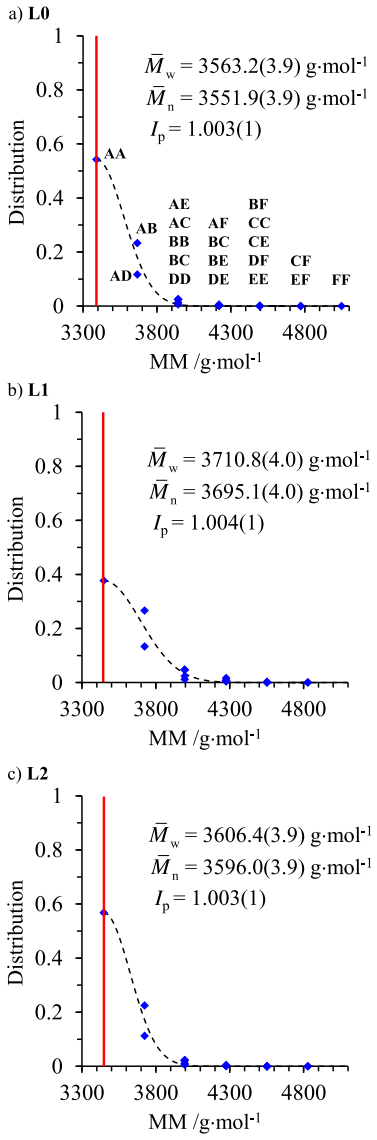

Fig. 21. Computed distributions of the various oligomers (blue diamonds) in the monodisperse (red line) and polydisperse dendrimers for a) poly-**L0** ($\alpha_{\mathbf{L0}}$ = 9.7%), b) poly-**L1** ($\alpha_{\mathbf{L1}}$ = 15.0%) and c) poly-**L2** ($\alpha_{\mathbf{L2}}$ = 9.0%). $\bar{M}_n$ is the predicted number average molecular weight, $\bar{M}_w$ is the weight average molecular weight and $I_p = \bar{M}_w/\bar{M}_n$ is the polydispersity index (see Appendix 4 in the Supporting Information). Detailed calculations using error propagation along the non-linear least square procedure leading to $\alpha_{\mathbf{Lk}}$, followed by mathematical reconstruction show that absolute errors on $\bar{M}_n$ and $\bar{M}_w$ are about 4 g/mol, whereas I_p are predicted within the ±0.001 range.

lar dipolar interactions for the stabilization of unidirectional nematic arrangement for the ligands, which is transformed into bi-dimensional smectic A arrangement for the complexes due to the implementation of large transverse electric dipole moments. The replacement of nitrate counter-anions in [**Lk**Eu(NO$_3$)$_3$] with hexafluoroacetylacetonato anions in [**Lk**Eu(hfac)$_3$] induces some subtle changes within the smectic phase as a result of (i) the lack of dimerization for the latter complexes and (ii) the additional operation of intermolecular interactions. With this in mind, it was attractive to convert some deleterious competitive esterification reactions encountered during the multistep synthesis of the dendrimers into an advantage for inducing controlled chemical pressure via the dispersion of structural defects into the final samples. Despite the low polydispersity indexes characterizing the distributions in the polydisperse dendrimers poly-**L0**-poly-**L2** and

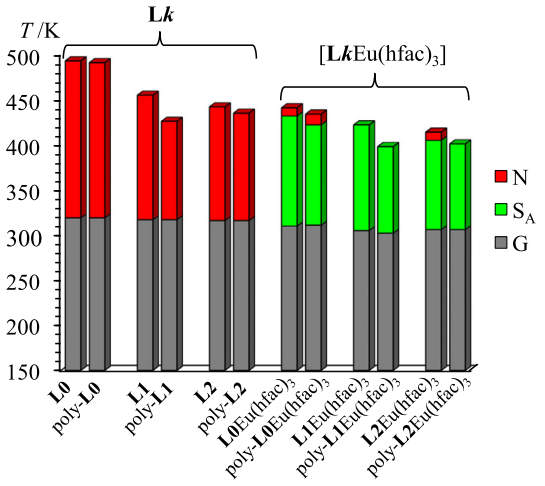

Fig. 22. Comparison of mesomorphic ranges and observed thermotropic mesophases for **Lk** *versus* poly-**Lk** and [**Lk**Eu(hfac)$_3$] *versus* poly-[**Lk**Eu(hfac)$_3$] (**Lk** = **L0**–**L2**; S$_A$ = smectic A phase, N = nematic phase, G = glassy state; scan rate 10 K/min).

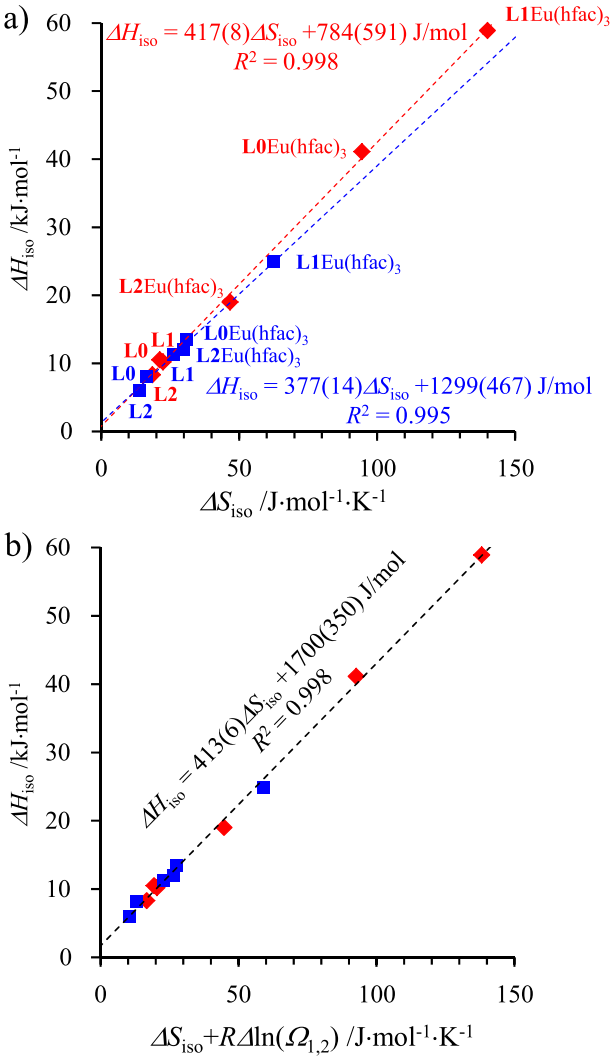

Fig. 23. Plots of enthalpy *versus* entropy values for the isotropization processes occurring in monodisperse (red diamonds) and polydisperse (blue squares) ligands **Lk** and complexes [**Lk**Eu(hfac)$_3$] according to a) Eq. (8) and b) Eq. (9) (R^2 = coefficient of determination) [56c].

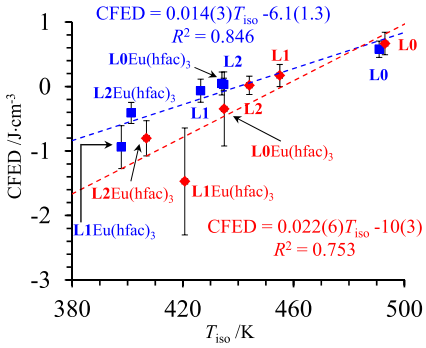

Fig. 24. Cohesive Gibbs free energy densities CFED *versus* isotropization temperature T_{iso} for he monodisperse (red diamonds) and polydisperse (blue squares) ligands **L*k*** and complexes [**L*k*** Eu(hfac)$_3$] using T^{ref}_{mono} = 442.4 K and T^{ref}_{poly} = 430.9 K as the reference temperatures (R^2 = coefficient of determination; units: 1.0 J·cm^{-3} = 1.0 MPa).

their corresponding europium complexes poly-[**L*k*** Eu(hfac)$_3$] ($1.0029 \leqslant I_p \leqslant 1.0043$), the latter chemical perturbation is unique among those considered here as it is able to significantly shift the phase boundary of the isotropization processes (Fig. 24). The analysis of the isotropization enthalpies and entropies within the frame of Khakhel's theory of extra-thermodynamic *H*/*S* compensation suggests that polydispersion noticeably reduces the (supra)-molecular packing in the mesophases, which make them less sensitive to chemical perturbation induced by specific molecular modifications (methylation of terminal cyanobiphenyls or metal complexation to the tridentate binding unit). In other words, the larger the polydispersity, the lower the sensitivity of the system to minor chemical perturbations, which justifies the adage saying that the properties of liquid crystals are easier to be tuned when they have been carefully purified... To summarize, the investigated lanthanidomesogens represent a proof-of-concept for the rational exploitation of phase boundaries deduced from plots of cohesive Gibbs free energy *versus* transition temperatures. Microscopic perturbations (i.e. chemical perturbations) can be manipulated as pressure increments, and their magnitudes quantitatively control the temperature domain of existence of thermotropic liquid crystals as it is found in standard *P*-*T* diagrams. This approach is quite general and may be profitable for the design of both organic and 'inorganic' thermotropic liquid crystals [20,24].

Acknowledgments

This work is supported through grants from the Swiss National Science Foundation. S.P. thanks "La Ligue contre le Cancer", Institut National de la Santé et de la Recherche Médicale (INSERM) for financial support in France. The work in France was carried out within the European COST action D38.

Appendix A. Supplementary data

Supplementary data associated with this article can be found, in the online version, at http://dx.doi.org/10.1016/j.ccr.2016.11.013.

References

[1] (a) G. Friedel, Ann. Phys. 18 (1922) 273–474;
(b) D. Dunmur, T. Sluckin, Soap, Science, and Flat-screen TVs: A History of Liquid Crystals, Oxford University Press, 2011.
[2] P.J. Flory, Spatial Configuration of Macromolecular Chains in Nobel Lectures in Chemistry, in: S. Forsen (Ed.), World Scientific Publishing Co, Singapore, 1993.
[3] P.G. de Gennes, Angew. Chem. Int. Ed. 31 (1992) 842–845.
[4] B. Bahadur (Ed.), Liquid Crystals Application and Uses, vol. 1, World Scientific Publishing Co, Singapore, 1990.
[5] R. Shashidhar, G. Venkatesh, J. Phys. Colloq. C3 (40) (1979) 396–400.
[6] P.W. Atkins, J. de Paula, Physical Chemistry, ninth ed., W. H. Freeman and Company, New York, 2010, p. 147.
[7] (a) D. Guillon, Struct. Bond. 95 (1999) 41–82;
(b) S. Diele, Curr. Opin. Coll. Int. Sci. 7 (2002) 333–342;
(c) J.W. Goodby, I.M. Saez, S.J. Cowling, V. Görtz, M. Draper, A.W. Hall, S. Sia, G. Cosquer, S.-E. Lee, E.P. Raynes, Angew. Chem. Int. Ed. 47 (2008) 2754–2787;
(d) T. Wöhrle, I. Wurzbach, J. Kirres, A. Kostidou, N. Kapernaum, J. Litterscheidt, J.C. Haenle, P. Staffeld, A. Baro, F. Giesselmann, S. Laschat, Chem. Rev. 116 (2016) 1139–1241.
[8] (a) C.T. Imrie, P.A. Henderson, Chem. Soc. Rev. 36 (2007) 2096–2124;
(b) C.V. Yelamaggad, I. Shashikala, Q. Li, Chem. Mater. 19 (2007) 6561–6568;
(c) P.N. Nelson, H.A. Ellis, Dalton Trans. 41 (2012) 2632–2638.
[9] K.E. Rowe, D.W. Bruce, J. Mater. Chem. 8 (1998) 331–341.
[10] (a) L. Onsager, Ann. N. Y. Acad. Sci. 51 (1949) 627–659;
(b) G.J. Vroege, H.N.W. Lekkerkerker, Rep. Prog. Phys. 55 (1992) 1241–1309.
[11] (a) W. Maier, A. Saupe, Z. Naturforsch. A 13a (1959) 564–570;
(b) W. Maier, A. Saupe, Z. Naturforsch. A 14a (1959) 882–900;
(c) W. Maier, A. Saupe, Z. Naturforsch. A 15a (1960) 287–292;
(d) A. Saupe, Angew. Chem. Int. Ed. 7 (1968) 97–118;
(e) G.R. Luckhurst, C. Zannoni, Nature 267 (1977) 412–414.
[12] A. Skoulios, D. Guillon, Mol. Cryst. Liq. Cryst. 165 (1988) 317–332.
[13] D. Guillon, A. Skoulios, J. Phys. 37 (1976) 797–800.
[14] K.J. Toyne, Thermotropic liquid crystals, in: G.W. Gray (Ed.), Critical Report on Applied Chemistry, vol. 22, 1987, pp. 28–63.
[15] E. Terazzi, S. Suarez, S. Torelli, H. Nozary, D. Imbert, O. Mamula, J.-P. Rivera, E. Guillet, J.-M. Bénech, G. Bernardinelli, R. Scopelliti, B. Donnio, D. Guillon, J.-C.G. Bünzli, C. Piguet, Adv. Funct. Mater. 16 (2006) 157–168.
[16] A. Escande, L. Guénée, H. Nozary, G. Bernardinelli, F. Gumy, A. Aebischer, J.-C.G. Bünzli, B. Donnio, D. Guillon, C. Piguet, Chem. Eur. J. 13 (2007) 8696–8713.
[17] C. Piguet, J.-C.G. Bünzli, B. Donnio, D. Guillon, Chem. Commun. (2006) 3755–3768.
[18] (a) C. Tschierske, Annu. Rep. Prog. Chem. Sect. C 97 (2001) 191–267;
(b) C. Tschierske, Top. Curr. Chem. 318 (2012) 1–108.
[19] (a) M.L. Huggins, J. Chem. Phys. 9 (1941) 440;
(b) P.J. Flory, J. Chem. Phys. 9 (1941) 660–661;
(c) D.R. Paul, S. Newman (Eds.), Polymer Blends, vol. 2, Academic Press, New York, San Francisco, London, 1978, pp. 25–32 and 116–121.
[20] S. Guerra, T. Dutronc, E. Terazzi, L. Guénée, C. Piguet, Phys. Chem. Chem. Phys. 18 (2016) 14479–14494.
[21] (a) J.H. Hildebrand, R.L. Scott, The Solubility of Nonelectrolytes, third ed., Reinhold Pub Group, New York, 1950;
(b) R.F. Fedors, Polym. Eng. Sci. 14 (1974) 147–154;
(c) A.F.M. Barton, Handbook of Solubility Parameters and Other Cohesion Parameters, second ed, vol. 127, CRC Press, 1991.
[22] F.T. Trouton, Philos. Mag. 18 (1884) 54–57.
[23] (a) T. Dutronc, E. Terazzi, L. Guénée, K.-L. Buchwalder, A. Spoerri, D. Emery, J. Mareda, S. Floquet, C. Piguet, Chem. Eur. J. 19 (2013) 8447–8456;
(b) T. Dutronc, E. Terazzi, C. Piguet, RSC Adv. 4 (2014) 15740–15748.
[24] T. Dutronc, E. Terazzi, L. Guénée, K.-L. Buchwalder, S. Floquet, C. Piguet, Chem. Eur. J. 22 (2016) 1385–1391.
[25] (a) Y.P. Piryatinskii, O.V. Yaroshchuk, Opt. Spectrosc. 92 (2002) 517–523;
(b) B. Jaishi, P. Mandal, R. Dabowki, Opto-Electron. Rev. 18 (2010) 111–120;
(c) N. Bielejewska, E. Chrzumnicka, R. Stoarki, D. Bauman, Opto-Electron. Rev. 18 (2010) 197–207;
(d) Market Research Report on Global and Chinese 4-cyanobiphenyl (CAS 2920-38-9) Industry, 2009–2019, Prof. Research Rep., 2014, PR 601577, pp. 1–150.
[26] G.W. Gray, K.J. Harrison, J.A. Nash, Electron. Lett. 9 (1973) 130–131.
[27] (a) A.C. Griffin, J.F. Johnson, Liquid Crystals and Ordered Fluids, vol. 4, Plenum Press, New York London, 1984;
(b) P.J. Collings, M. Hird, Introduction to Liquid Crystals: Chemistry and Physics, in: G.W. Gray, J.W. Goodby (Eds.), Taylor and Francis Ltd, London, Bristol, 1997;
(c) D. Demus, J.W. Goodby, G.W. Gray, H.-W. Spiess, V. Vill (Eds.), Handbook of Liquid Crystals, vols. 1 and 2A, Wiley-CVH, Weinheim, 1998.
[28] V.P. Shibaev, L. Lam, Liquid Crystalline and Mesomorphic Polymers, Springer Verlag, New York, 1994 (Chapter 3).
[29] (a) T. Cardinaels, K. Driesen, T.N. Parac-Vogt, B. Heinrich, C. Bourgogne, D. Guillon, B. Donnio, K. Binnemans, Chem. Mater. 17 (2005) 6589–6598;
(b) I.S. Shashikala, D.W. Bruce, Dalton Trans. (2008) 1128–1131;
(c) E. Terazzi, C. Bourgogne, R. Welter, J.-L. Gallani, D. Guillon, G. Rogez, B. Donnio, Angew. Chem. Int. Ed. 47 (2008) 490–495;
(d) A. Pana, F.L. Chiriac, M. Secu, I. Pasuk, M. Ferbinteanu, M. Micutz, V. Circu, Dalton Trans. 44 (2015) 14196–14199.
[30] (a) S.V. Eliseeva, J.-C.G. Bünzli, New J. Chem. 35 (2011) 1165–1176;
(b) L. Sorace, C. Benelli, D. Gatteschi, Chem. Soc. Rev. 40 (2011) 3092–3104;
(c) J. Luzon, R. Sessoli, Dalton Trans. 41 (2012) 13556–13567;
(d) J. Lehr, P.D. Beer, S. Faulkner, J.J. Davis, Chem. Commun. 50 (2014) 5678–5687.
[31] (a) A.M. Giroud-Godquin, P.M. Maitlis, Angew. Chem. Int. Ed. Engl. 30 (1991) 375–402;
(b) S.A. Hudson, P.M. Maitlis, Chem. Rev. 93 (1993) 861–885;
(c) D.W. Bruce, J. Chem. Soc. Dalton Trans. (1993) 2983–2989;
(d) J.L. Serrano (Ed.), Metallomesogens Synthesis, Properties, and Applications, VCH, Weinheim, 1996;
(e) A.-M. Giroud-Godquin, Coord. Chem. Rev. vols. 178–180 (1998) 1485;

(f) P. Espinet, Gold Bull. 32 (32) (1999) 127–134;
(f) B. Donnio, D.W. Bruce, Struct. Bond. 95 (1999) 194–247;
R.W. Date, E. Fernandez Iglesias, K.E. Rowe, J.M. Elliott, D.W. Bruce, Dalton Trans. (2003) 1914–1931;
(h) K. Binnemans, J. Mater. Chem. 19 (2009) 448–453.

[32] (a) L. Douce, A. El-ghayouri, A. Skoulios, R. Ziessel, Chem. Commun. (1999) 2033–2034;
(b) A. Pegenau, T. Hegmann, C. Tschierske, S. Diele, Chem. Eur. J. 5 (1999) 1643–1660;
(c) M.C. Barral, R. Jumenez-Aparicio, J.L. Priego, E.C. Royer, M.R. Torres, F.A. Urbanis, Inorg. Chem. Commun. 2 (1999) 153–155;
(d) S.T. Trzaska, H.-F. Hsu, T.M. Swager, J. Am. Chem. Soc. 121 (1999) 4518–4519;
(e) M.-A. Guillevic, D.W. Bruce, Liq. Cryst. 27 (2000) 153–156;
(f) E. Cavero, S. Uriel, P. Romero, J.L. Serrano, R. Gimenez, J. Am. Chem. Soc. 129 (2007) 11618–11698;
(g) M. Seredyuk, M.C. Munoz, V. Ksenofontov, P. Gütlich, Y. Galyametdinov, J. A. Real, Inorg. Chem. 53 (2014) 8442–8454.

[33] (a) For comprehensive reviews on lanthanidomesogens see K. Binnemans, C. Görller-Walrand Chem. Rev. 102 (2002) 2303–2346;
(b) K. Binnemans, Lanthanidomesogens, in: J.-C.G. Bünzli, V.K. Pecharsky (Eds.), Handbook on the Physics and Chemistry of Rare Earths, Elsevier Science, Amsterdam, 2013, pp. 1–158.

[34] K. Binnemans, Y.G. Galyametdinov, R. Van Deun, D.W. Bruce, S.R. Collinson, A. P. Polishchuk, I. Bikchantaev, W. Haase, A.V. Prosvirin, L. Tinchurina, U. Litvinov, A. Gubajdullin, A. Rakhmatullin, K. Uytterhoeven, L. Van Meervelt, J. Am. Chem. Soc. 122 (2000) 4335–4344.

[35] (a) C. Piechocki, J. Simon, J.J. André, D. Guillon, A. Skoulios, P. Weber, Chem. Phys. Lett. 122 (1985) 124–128;
(b) T. Komatsu, K. Ohta, T. Fujimoto, I. Yamamoto, J. Mater. Chem. 4 (1994) 537–540;
(c) T. Toupance, P. Bassoul, L. Mineau, J. Simon, J. Phys. Chem. 100 (1996) 11704–11710;
(d) K. Ban, K. Nishizawa, K. Ohta, A. van de Craats, J.M. Warman, I. Yamamoto, H. Shirai, J. Mater. Chem. 11 (2001) 321–331;
(e) J. Sleven, C. Görller-Walrand, K. Binnemans, Mater. Sci. Eng. C C18 (2001) 229–238;
(f) F. Maeda, K. Hatsusaka, K. Ohta, M. Kimura, J. Mater. Chem. 13 (2003) 243–251;
(g) K. Binnemans, J. Sleven, S. De Feyter, F.C. De Schryver, B. Donnio, D. Guillon, Chem. Mater. 15 (2003) 3930–3938.

[36] E. Terazzi, S. Torelli, G. Bernardinelli, J.-P. Rivera, J.-M. Bénech, C. Bourgogne, B. Donnio, D. Guillon, D. Imbert, J.-C.G. Bünzli, A. Pinto, D. Jeannerat, C. Piguet, J. Am. Chem. Soc. 127 (2005) 888–903.

[37] N.S.S. Kumar, M.Z. Shafikov, A.C. Whitwood, B. Donnio, P.B. Karadakov, V.N. Kozhevnikov, D.W. Bruce, Chem. Eur. J. 22 (2016) 8215–8233.

[38] K. Binnemans, R. Van Deun, D.W. Bruce, Y.G. Galyametdinov, Chem. Phys. Lett. 300 (1999) 509–514.

[39] (a) B. Dardel, D. Guillon, B. Heinrich, R. Deschenaux, J. Mater. Chem. 11 (2001) 2814–2831;
(b) R. Deschenaux, S. Campidelli, Helv. Chim. Acta 84 (2001) 589–593;
(c) S. Campidelli, R. Deschenaux, J.-F. Eckert, D. Guillon, J.-F. Nierengarten, Chem. Commun. (2002) 656–657;
(d) S. Campidelli, E. Vázquez, D. Milic, M. Prato, J. Barberá, D.M. Guldi, M. Marcaccio, D. Paolucci, F. Paolucci, R. Deschenaux, J. Mater. Chem. 14 (2004) 1266–1272;
(e) S. Campidelli, J. Lenoble, J. Barberá, F. Paolucci, M. Marcaccio, D. Paolucci, R. Deschenaux, Macromolecules 38 (2005) 7915–7925;
(f) S. Campidelli, L. Pérez, J. Rodriguez-López, J. Barberá, F. Langa, R. Deschenaux, Tetrahedron 62 (2006) 2115–2122;
S. Campidelli, E. Vázquez, D. Milic, J. Lenoble, C. Atienza Castellanos, G. Sarova, D.M. Guldi, R. Deschenaux, M. Prato, J. Org. Chem. 71 (2006) 7603–7610;
J. Lenoble, S. Campidelli, N. Maringa, B. Donnio, D. Guillon, N. Yevlampieva, R. J. Am. Chem. Soc. 129 (2007) 9941–9952.

[40] (a) I.M. Saez, J.W. Goodby, Liq. Cryst. 26 (1999) 1101–1105;
(b) I.M. Saez, J.W. Goodby, J. Mater. Chem. 15 (2005) 26–40.

[41] (a) S. Fein, M. Auzias, A. Sondenecker, L. Vieille-Petit, B. Guintchin, N. Maringa, G. Suess-Fink, J. Barberà, R. Deschenaux, Chm. Mater. 20 (2008) 1340–1343;
(b) A. Pitto-Barry, N.P.E. Barry, V. Russo, B. Heinrich, B. Donnio, B. Therrien, R. Deschenaux, J. Am. Chem. Soc. 136 (2014) 17616–17625.

[42] (a) R. Deschenaux, B. Donnio, D. Guillon, New J. Chem. 31 (2007) 1064–1073;
(b) B. Donnio, S. Buathong, I. Bury, D. Guillon, Chem. Soc. Rev. 36 (2007) 1495–1513.

[43] (a) E. Terazzi, B. Bocquet, S. Campidelli, B. Donnio, D. Guillon, R. Deschenaux, C. Piguet, Chem. Commun. (2006) 2922–2924;
(b) T.B. Jensen, E. Terazzi, B. Donnio, D. Guillon, C. Piguet, Chem. Commun. (2008) 181–183;
(c) E. Terazzi, A. Zaïm, B. Bocquet, J. Varin, L. Guénée, T. Dutronc, J.-F. Lemonnier, S. Floquet, E. Cadot, B. Heinrich, B. Donnio, C. Piguet, Eur. J. Inorg. Chem. (2013) 3323–3333.

[44] T.B. Jensen, E. Terazzi, K. Buchwalder, L. Guénée, H. Nozary, K. Schenk, B. Heinrich, B. Donnio, D. Guillon, C. Piguet, Inorg. Chem. 49 (2010) 8601–8619.

[45] M.J. Hudson, M.G.B. Drew, M.R.S. Foreman, C. Hill, N. Huet, C. Madic, T.G.A. Youngs, J. Chem. Soc. Dalton Trans. (2003) 1675–1685.

[46] A. Zaïm, H. Nozary, L. Guénée, C. Besnard, J.-F. Lemonnier, S. Petoud, C. Piguet, Chem. Eur. J. 18 (2012) 7155–7168.

[47] D. Munro, Chem. Brit. 13 (1977) 100–105.

[48] L. Liu, Q.-X. Guo, Chem. Rev. 101 (2001) 673–695.

[49] C. Piguet, Dalton Trans. 40 (2011) 8059–8071.

[50] H. Nozary, C. Piguet, P. Tissot, G. Bernardinelli, J.-C.G. Bünzli, R. Deschenaux, D. Guillon, J. Am. Chem. Soc. 120 (1998) 12274–12288.

[51] G.R. Choppin, Z.M. Wang, Inorg. Chem. 36 (1997) 249–252.

[52] The rate of Einstein spontaneous emission between two states with quantum numbers J and J', A(ΨJ, ΨJ) is given by $A(\Psi_J, \Psi'_{J'}) = \frac{1}{\tau_{rad}} = \frac{64\pi^4\tilde{\nu}^3}{3h(2J+1)}\left[\frac{n(n^2+2)^2}{9}D_{ED} + n^3 D_{MD}\right]$ where $\tilde{\nu}$ is the average energy of the transition in cm^{-1}, h Planck's constant, and $(2J+1)$ the degeneracy of the initial (emitting) state; the expressions involving the refractive index n are known as the Lorentz local field corrections and D_{ED} and D_{MD} are the electric and magnetic dipole oscillator strengths, respectively (in $esu^2 \cdot cm^2$);
(a) A. Einstein, Physik. Z. 18 (1917) 121;
(b) A. Pais, Rev. Mod. Phys. 49 (1977) 925–938;
(c) C. Görller-Walrand, K. Binnemans, Spectral Intensities of f-f Transitions, in: K.A. Gschneidner, L. Eyring (Eds.), Handbook on the Physics and Chemistry of Rare Earths, vol. 25, Elsevier Science, Amsterdam, 1998, pp. 101–264.

[53] (a) A. Aebischer, F. Gumy, J.-C.G. Bünzli, Phys. Chem. Chem. Phys. 11 (2009) 1346–1353;
(a) J.-C.G. Bünzli, A.-S. Chauvin, H.K. Kim, E. Deiters, S.V. Eliseeva, Coord. Chem. Rev. 254 (2010) 2623–2633.

[54] (a) E. Terazzi, G. Rogez, J.-L. Gallani, B. Donnio, J. Am. Chem. Soc. 135 (2013) 2708–2722;
(b) S. Floquet, E. Terazzi, A. Hijazi, L. Guénée, C. Piguet, E. Cadot, New J. Chem. 36 (2012) 865–868.

[55] L. Babel, T.N.Y. Hoang, L. Guénée, C. Besnard, T.A. Wesolowski, M. Humbert-Droz, C. Piguet, Chem. Eur. J. 22 (2016) 8113–8123.

[56] (a) O.A. Khakhel', Chem. Phys. Lett. 421 (2006) 464–468;
(b) O.A. Khakhel', T.P. Romashko, Y.E. Sakhno, J. Phys. Chem. B 111 (2007) 7331–7335;
(c) O.A. Khakhel', T.P. Romashko, J. Phys. Chem. A 120 (2016) 2035–2040.

[57] D.H. Leung, R.G. Bergman, K.N. Raymond, J. Am. Chem. Soc. 130 (2008) 2798–2805.

[58] (a) D.M. Ford, J. Am. Chem. Soc. 127 (2005) 16167–16170;
(b) D.M. Ford, Adsorption 11 (2005) 271–277.

[59] (a) J.-S. Hu, L.-Q. Yang, X. Zhang, Z.-W. Song, Liq. Cryst. 37 (2010) 1259–1268;
(b) J.-S. Hu, X. Zhang, Y.-G. Jia, Q.-B. Meng, Liq. Cryst. 39 (2012) 121–131.